Modelling Gravitational Settling of Heavy Elements in the Solar Chromosphere

Iselin Bø
Master's thesis
Institute of Theoretical Astrophysics
University of Oslo

December 2008

Preface

This thesis is a collaboration between Stefano Pucci and the undersigned. The main part of this collaboration has been the implementation of the code which successively has been used to produce the results. The chapters 2 and 3, which describe the physical problem and the work with the code in detail, are common, and therefore included in both theses. After finishing the main structure of the code, the work was divided into two main directions. The first one, carried out by Pucci, is a study of minor constituents in a chromosphere where the hydrogen background flows outwards, and the latter, carried out by the undersigned, is a study of minor constituents in a chromosphere without any net outflow of hydrogen.

I want to thank my supervisor Øystein Lie-Svendsen for his indispensable guidance and impressive patience during the work with this thesis. I also want to thank Vibeke Riekeles for proof reading, and many thanks to my sister Lilja and to Kirsten and Giovannella for taking so good care of my daughter Erika.

Oslo, December 2008

Iselin Bø

List of Tables

Contents

Chapter 1

Introduction

The composition of the sun and the solar atmosphere is important for the understanding of the dynamics in and between the different solar atmosphere layers. When comparing the observed elemental abundances in the upper solar atmosphere and the solar wind with the photospheric abundances, systematic anomalies that seem to follow the first ionisation potential (FIP) of the elements, has been found. Observations show a fractionation of the elements according to FIP, where the abundance ratio between elements with FIP $< 10eV$ (low FIP elements) and elements with FIP $> 10eV$ (high FIP elements) is enhanced. Some studies of this topic are briefly presented below.

We will discuss the elemental abundances both relative to the hydrogen and to the oxygen abundance. We label the abundance of an element X relative to hydrogen as the *absolute abundance*,

$$\mathcal{A} = \mathcal{A}(\mathrm{X}) = \frac{N_{\mathrm{X}}}{N_{\mathrm{H}}} \ , \tag{1.1}$$

and the abundance of the element X relative to oxygen (or another minor element in the sun) as the *relative abundance*,

$$\mathcal{R} = \mathcal{R}(\tfrac{\mathrm{X}}{\mathrm{O}}) = \frac{N_{\mathrm{X}}}{N_{\mathrm{O}}} \ , \tag{1.2}$$

where N_{X} is the total (neutral + ionised) number density of the minor element, N_{H} is the total hydrogen number density, and N_{O} is the total oxygen number density. We then define the *FIP fractionation* of a certain element as the ratio between the relative abundance measured in a particular structure of the upper solar atmosphere (i.e. in a coronal hole, a polar plume, a streamer, etc.) and the relative abundance in the photosphere,

$$\mathcal{F} = \frac{\mathcal{R}^{upper\ atmosphere}}{\mathcal{R}^{photosphere}} \ . \tag{1.3}$$

The photosphere The first measurements of the solar atmosphere composition were done by Russell (1929) who identified 56 solar elements and determined their elemental abundances by studying the solar photospheric spectra. A review of the photospheric elemental abundance observations was done by Anders and Grevesse (1989) (with some corrections in Grevesse and Sauval (1998)). Their study constitutes the most frequently used reference for such abundances. To derive the photospheric abundances, both spectroscopy and a special kind of meteorites called CI carbonaceous chondrites are used. The spectroscopic method (Biemont and Grevesse, 1977)(Gray, 2005) consists in comparing the equivalent width of an absorption line with a theoretically generated 'curve of growth'.

The equivalent width is defined by

$$W_\nu = \int_0^\infty \frac{F_\nu - F_c}{F_c}\, d\nu \ , \tag{1.4}$$

where F is the energy flux per unit frequency, ν is the frequency of the line, and c refers to the continuum level. The energy flux is given by the integral of the radiation intensity I_ν, which describes how the energy generated in the photosphere is transferred by radiation to the outer layers.

The curve of growth is the relation between the equivalent width and the number of absorbing atoms. In order to construct the curve of growth one has to determine theoretically the equivalent width, i.e. to integrate the intensity over the whole layer where the photospheric spectra is generated. This means that one has to know the temperature and the density as functions of the optical depth. The line opacity, which is also necessary to determine the equivalent width, is proportional to three factors: First, the population of the lower level of the transition, which in turn is directly related to the absolute abundance of the element $\mathcal{A}$, second, the absorption coefficient at the centre of the line and the function that determines the shape of the line profile, both depending on the Doppler broadening of the line, and third, the oscillator strength or the transition probability of the line. For further details see Gray (2005).

The abundances derived from meteorites were initially determined with by far better accuracy than the ones derived through the photospheric spectra. However, with an increasing resolution of the photospheric spectra and more accurate atomic data (mainly for the determination of the transition probabilities), the uncertainties related to the spectroscopic method were reduced. The abundances derived with the two methods now correspond very well. The photospheric abundances relevant for the present work are listed in table 1.1. These values are taken from Grevesse and Sauval (1998) for all elements except oxygen, whose value is taken from Asplund et al. (2004).

	$FIP(eV)$	$\log A$	N_x/N_H
H	13.6	12.00	1
O	13.6	8.66 ± 0.05 [1]	$(4.1 - 5.1) \times 10^{-4}$ [1]
Ne	21.6	8.08 ± 0.06 [2]	$(1.1 - 1.4) \times 10^{-4}$ [2]
Mg	7.6	7.58 ± 0.05	$(3.4 - 4.3) \times 10^{-5}$
Si	8.1	7.55 ± 0.05	$(3.2 - 4.0) \times 10^{-5}$
Fe	7.9	7.50 ± 0.05	$(2.8 - 3.6) \times 10^{-5}$

Table 1.1: First ionisation potentials and elemental abundances in the solar photosphere (Grevesse and Sauval, 1998). The abundances in column two are given by $\log A = 12.00 + \log \frac{N_x}{N_H}$

A special note has to be given to the volatile elements, such as C, N, O and the noble gases. They are largely lost in meteorites, the lines from the noble gases are absent in the photospheric spectra, and accurate atomic data for C, N and O have been missing. These facts lead to severe difficulties in determining the photospheric abundances for the volatile elements. However, the improvement of solar models and the inversion of helioseismic data have made it possible to determine the solar helium abundance. Widing (1997) estimated the photospheric neon abundance using data from an emerging magnetic flux region, where he assumed that the composition of this emerging gas was the same as in the photosphere. He measured the Ne/Mg abundance ratio, and by using the well known photospheric magnesium abundance, he derived the abundance of neon.

Since the majority of the FIP fractionation observations study the minor constituents of the solar atmosphere with an emphasis on the relative abundances with respect to oxygen, it is important to notice the existing controversy around the photospheric oxygen abundance. Asplund et al. (2004) have given a new estimation of the photospheric oxygen abundance which is approximately 30% lower than the same value given by Grevesse and Sauval (1998). The new estimate for this element abundance is based on 3D hydrodynamic models (compared to the earlier 1D models), which compute the atomic level populations. These are then applied to the solar absorption lines.

The upper solar atmosphere and the solar wind It was only when the spacecraft technology permitted to perform observations with telescopes

[1]The oxygen abundance is taken from Asplund et al. (2004)

[2]The neon abundance is measured in emerging magnetic flux events, which is assumed to have photospheric composition. (Widing, 1997).

on board satellites that astrophysicists started to study the elemental abundances of the upper solar atmosphere and the solar wind. Hence, the comparison between the photosphere and the other layers of the solar atmosphere became possible. The coronal abundances are generally determined by spectroscopic means. The solar wind abundances and solar energetic particles from solar flares are on the other hand determined with in-situ measurements. By determining the charge and mass of the flow particles, it is possible to detect the occurrence rate of each particle type. For the photospheric abundances the spectroscopic method is based on a comparison between the line intensity and the continuum, while in the corona one has to compare the absorption line of the element in interest with the absorption line of another element. Thereby, the relative abundance of the first element with respect to the second is derived.

One of the earliest observations of the FIP fractionation phenomena took place when Mogro-Campero and Simpson (1972) found an abundance enhancement of low FIP elements relative to oxygen (FIP = 13.6 eV) from in-situ measurements of solar energetic particles on the OGO-5 satellite. Thirteen years later, Meyer (1985) analysed all the existing spacecraft observations of the heavy element composition in the solar corona, solar wind and solar energetic particles. He found that they all had very similar compositions, and that low FIP/high FIP abundance ratios were enhanced compared to the photosphere. Later measurements of the solar wind with the SWICS mass spectrometer on Ulysses by von Steiger et al. (1995), showed evidence for differences in the FIP fractionation between the slow and the fast solar wind. Compared to the corresponding ratio of the photospheric abundances, the low to high FIP abundance ratios were increased by a factor of 3 to 5 in the slow solar wind, while the same ratios in the fast solar wind were only increased by a factor of 1.5 to 2.

In the late 1980's and in the 1990's analyses of the upper atmosphere spectra within different regions of the solar surface brought difficulties to the interpretation of the FIP fractionation. Different abundance ratios were found in different regions of the upper atmosphere corresponding to different features of the magnetic field. Widing and Feldman (1989) derived relative abundances from an analysis of a prominence, flare and active region observed with the NRL spectroheliograms on Skylab. They found a strong correlation between the abundance variation and the magnetic field morphology. In a later study, based on measurements from the same instrument, Widing and Feldman (1992) determined elemental abundances in a coronal polar plume. They found that the relative abundance $\mathcal{R}(\frac{\mathrm{Mg}}{\mathrm{Ne}})$ between Mg and Ne was enhanced by a factor of ten compared to the corresponding photospheric ratio. Young (2005) determined a relative abundance of the same

ratio that was enhanced by a factor of 4 to 5, compared to the photosphere, in the quiet sun at temperatures $5.0 < \log(T/\mathrm{K}) < 6.1$.

With the launch of the SOHO satellite in 1995, high quality instruments (e.g. UVCS and SUMER) gave stronger Lyman lines than earlier and opened for more accurate observations of the hydrogen spectra from coronal structures. Hence, measurements of the absolute abundances in the corona were possible. Raymond et al. (1997a) studied a quiescent equatorial streamer and an active region streamer at a distance of $1.5R_\odot$ (1.5 solar radii) from the centre of the sun. They found abundance variations between these two streamers and within the equatorial streamer. The absolute oxygen abundance $\mathcal{A}(\mathrm{O})$ was depleted by an order of magnitude in the centre of the quiescent streamer compared to the photospheric value, while the absolute abundances $\mathcal{A}(\mathrm{Mg})$, $\mathcal{A}(\mathrm{Si})$ and $\mathcal{A}(\mathrm{Fe})$ of the low FIP elements magnesium, silicon and iron, were depleted by approximately a factor of 3, 7 and 3, respectively. $\mathcal{A}(\mathrm{O})$ in the active region streamer and in the streamer leg of the equatorial streamer were depleted by a factor of ~ 2 and ~ 3 respectively, while the low FIP abundances in the active region streamer and in the streamer leg were very similar to the photospheric values for all the low FIP elements except for silicon which was depleted by a factor of ~ 3 in the streamer leg of the quiescent streamer. The high depletion of oxygen in the streamer core was explained by gravitational settling. Very similar results were found in observations of the same equatorial streamer at larger heights by Raymond et al. (1997b).

White et al. (2000) introduced a new technique for the measurement of coronal absolute abundances, using the CDS instrument on SOHO together with bremsstrahlung radio data from the Very Large Array observatory. They measured the absolute iron abundance in a compact cool active region, and found the value $\mathcal{A}(\mathrm{Fe}) = 1.56 \times 10^{-4}$, which is more than four times the corresponding photospheric value.

Models During the last decades, a number of theoretical models have been made to simulate the physical processes in the upper solar atmosphere, trying to reproduce the observed elemental abundances. Considering the complexity of the physical quantities in the solar atmosphere (magnetic fields, temperature profile, gas fluxes etc), this is not an easy task. In fact, the fractionation processes in the solar atmosphere leading to the abundance variations according to FIP are not yet fully understood. We believe that the FIP fractionation process has its origin somewhere in the chromosphere where the low FIP elements become ionised, and many efforts have been made to try to explain the mechanism behind this abundance variation.

Hénoux (1998) reviewed theoretical studies of mechanisms leading to the FIP dependent abundance variation, including both models where the magnetic field plays, and *not* plays an 'active' role. In the first class of models, the magnetic field is the key factor for the fractionation process to take place. Whereas the low FIP elements become ionised already in the lower layer of the atmosphere, the high FIP elements remain neutral. These neutral, high FIP elements can therefore move perpendicularly to the field lines and escape the magnetic field. The low FIP elements on the other hand are forced to move along the field lines. Hence, the high and low FIP elements can have very different drift velocities due to the morphology and the dynamic of the magnetic field. One example of models from this class is a model by Vauclair (1996). He modelled the solar atmosphere with an ascending horizontal magnetic field that was able to lift the ionised low FIP elements to higher layers. Because of gravity, the neutral high FIP elements settled down crossing the magnetic field lines. Hence an enrichment of low FIP elements relative to high FIP elements in the upper layers of the solar atmosphere was produced. The models developed by von Steiger and Geiss (1989) and Henoux and Somov (1997) are other examples of models with a magnetic field that plays an active role in the fractionation process. In the second class of models, the magnetic field is 'passive'. This means that the magnetic field, if present at all, is only present in order to specify the flow of the ions. The second class models explain the fractionation process by diffusion along field lines. Concrete examples of second class models are the ones developed by Marsch et al. (1995), Peter (1998) and Wang (1996). They highly depend on the choice of the boundary conditions and therefore differ mainly due to different choices of these conditions.

The present work In spite of the existing models claiming to explain the FIP fractionation processes (Peter, 1998), other models emphasise the need for a more detailed understanding of certain processes on the sun in order to obtain the complete picture. Hansteen et al. (1997) studied the coronal helium abundance in a numerical model with a collisionally dominated heat flux and found that the frictional coupling between neutral helium and the partially ionised hydrogen plasma had to be multiplied by a factor of 15 in order to create a force sufficiently large to counteract the gravitational force, that otherwise would not be able to pull out any helium from the solar chromosphere. Also the collision frequencies for the minor constituents silicon and oxygen (Lie-Svendsen and Esser, 2005) have to be 'artificially' enhanced in order to get a reasonable amount of these elements out in the solar wind. Hence, there are reasons to believe that some process is able

to keep the hydrogen gas and the trace gases well mixed through the whole chromospheric layer.

The two above examples tell us that there are still mechanisms that have to be fully understood. They both therefore constitute the motivation for the present chromospheric model.

In this work we model the gravitational settling of minor elements starting with a well mixed, 'closed' chromosphere, i.e. a chromosphere where all the elements have the same scale height as hydrogen in the beginning, and where no gas is able to enter from the transition region above. The hydrogen background does only have small velocities and there is no net outflow of hydrogen (no solar wind). We study the gravitational settling of O, Mg, Si, Ne and Fe when the ionisation processes, the pressure gradient, gravity, the electric field (generated by the electrons) and the collisions between the minor elements and hydrogen are included. The idea is to see if the Coulomb collisions are able to delay the gravitational settling of the low FIP elements in the upper part of the chromosphere, compared to the high FIP elements, in order to create an enhancement of the low to high FIP abundance ratio. We then assume that some mechanism should be able to transport this gas to the corona thus giving raise to the variation in elemental composition between the photosphere and the corona. It is important to note that for this to be possible, there need to be some regular mixing processes in the chromosphere, or else steady state will be reached and both high and low FIP elements will be strongly depleted according to their small scale heights compared to hydrogen.

Chapter 2

The model

We consider a slab of the solar atmosphere of a certain thickness and with a certain temperature profile. For simplicity we consider the atmosphere as a one dimensional system with plane parallel symmetry.

The atmosphere model consists of a pure hydrogen background (see section 4.1) and one of the trace elements (minor constituents) O, Ne, Mg, Si or Fe at the time. Only neutrals and singly ionised particles are included, and the hydrogen background is quasi neutral, i.e. the electron density is the same as the proton density.

The physical quantities are governed by the mass conservation (mass continuity equation) and the momentum equation (Newton's second law). No energy equation is solved, but a linear temperature profile is given. In this way we avoid the problems related to the coupling between the radiative transport equation and the hydrodynamic equations.

We consider a magnetic field with vertical magnetic flux lines and flow, in vertical direction only. Hence, since the contribution from the magnetic field is proportional to the vector product between the magnetic field and the velocity, we do not need to include any magnetic field term in the momentum equation.

We model the following equations

$$\frac{\partial n_i}{\partial t} + \frac{\partial}{\partial z}(n_i\ u_i) = n_j\ P_{ji} - n_i\ P_{ij} \tag{2.1}$$

$$\begin{aligned}\frac{\partial (n_i u_i)}{\partial t} + \frac{\partial}{\partial z}(n_i u_i u_i) = &-\frac{1}{m_i}\frac{\partial}{\partial z}(n_i k T) + g n_i + n_j u_j\ P_{ji} - n_i u_i P_{ij} \\ &+ \frac{n_i q_i}{m_i}\ E + \sum_{j \neq i} n_i \nu_{ij}(u_j - u_i)\end{aligned} \tag{2.2}$$

where the indexes i and j can take the values 1 or 2, representing neutral gas and ionised gas, respectively. n_i is the number density and u_i is the velocity of the species i. P_{12} is the ionisation rate and P_{21} the recombination rate, both discussed in section 2.1. m_i and q_i are the mass and the electric charge of the species i, respectively. E is the electric field (see section 2.4) and ν_{ij} is the collision frequency between the species i and j. The collision frequencies are treated in section 2.5. g is the gravitational acceleration, set to $g = -270$ m s^{-2}, T is the temperature (constant in time) and k is Boltzmann's constant. The derivatives in equation 2.1 and 2.2 are taken with respect to time t and height z. All the variables are in SI-units, if nothing else is specified.

We model the background with the same equations (2.1 and 2.2) as for the minor constituents, but for practical reasons we rewrite the momentum equation for neutral hydrogen and protons as

$$\frac{\partial(n_H u_H)}{\partial t} + \frac{\partial}{\partial z}(n_H u_H u_H) = -\frac{1}{m_H}\frac{\partial}{\partial z}(n_H kT) + g n_H + k_{mt}\ n_H\ n_p(u_p - u_H) + n_p u_p\ P_{21} - n_H u_H P_{12} \tag{2.3}$$

$$\frac{\partial(n_p u_p)}{\partial t} + \frac{\partial}{\partial z}(n_p u_p u_p) = -\frac{2}{m_p}\frac{\partial}{\partial z}(n_p kT) + g n_p + k_{mt}\ n_p\ n_H(u_H - u_p) + n_H u_H\ P_{12} - n_p u_p P_{21}\ . \tag{2.4}$$

The collisions between protons and neutral hydrogen are dominated by the charge transfer process, and due to Newton's third law, their collision rate coefficients k_{mt} are equal. This rate coefficient depends on the temperature, and we have adopted the following relation between k_{mt} and T,

$$k_{mt} = k_{mt}(T) = 1 \times 10^{-14}\sqrt{\frac{T_H + T_p}{10^4\mathrm{K}}}\ , \tag{2.5}$$

in units m^3 s^{-1}, where the neutral hydrogen and proton temperatures, T_H and T_p, are both equal the electron temperature T. In order to check if this is a reasonable estimation of the collision frequency we have compared it with the values of the rate coefficient k_{mt} provided by Schultz et al. (2008). They give two values of k_{mt} in our temperature range, $k_{mt} = 1.59 \times 10^{-14}$ m^3 s^{-1} at $T = 7 \times 10^3$K and $k_{mt} = 1.82 \times 10^{-14}$ m^3 s^{-1} at $T = 1 \times 10^4$K. These values are higher than what equation 2.5 yields at the same temperatures, i.e. $k_{mt}(T = 7{\times}10^3\mathrm{K}) = 1.19{\times}10^{-14}$ m^3 s^{-1} and $k_{mt}(T = 1{\times}10^4\mathrm{K}) = 1.41{\times}10^{-14}$ m^3 s^{-1}, but they agree within an uncertainty of 30%. The factor two in the pressure term for protons is due to the electric field, described in section 2.4.

2.1 Ionisation rates

The ionisation rate P_{ij} can be written as the sum of the radiative ionisation R_{ij} and the collisional ionisation C_{ij},

$$P_{ij} = R_{ij} + C_{ij} \ . \tag{2.6}$$

For the hydrogen background, the collisional ionisation rate is almost always negligible, while only collisional ionisation is included for the minor constituents except for oxygen, where we also take into account the charge transfer with hydrogen (see section 2.3). The collisional ionisation rate for oxygen is negligible.

2.1.1 Hydrogen radiative ionisation

Radiative ionisation occurs when atoms are ionised by photon absorption. The photon energy $h\nu$ has to be greater than or equal to $h\nu_0$, where ν_0 is the threshold frequency of the ionising atom. The threshold frequency is directly related to the first ionisation potential I for each element,

$$\nu_0 = \frac{I}{h} \ . \tag{2.7}$$

The photoionisation rate for hydrogen is taken from Rutten (1999),

$$R_{12} = 4\pi \int_{\nu 0}^{\infty} \frac{\sigma_{12}(\nu)}{h\nu} J_\nu d\nu \ , \tag{2.8}$$

where ν is the radiation frequency, h is Planck's constant, J_ν is the source function and σ_{12} is given by

$$\sigma_{12} = \alpha_0 \left(\frac{\nu_0}{\nu}\right)^3 \ . \tag{2.9}$$

α_0 is the cross section at the threshold frequency ν_0.

To continue the evaluation of the integral in equation 2.8 without resolving the radiative transfer equation we need to specify the source function J_ν. As a first approximation we use

$$J_\nu = B_\nu = \frac{2h\nu^3}{c^2} \ \frac{1}{e^{h\nu/kT_{rad}} - 1} \tag{2.10}$$

where B_ν is the Planck function, c is the speed of light and T_{rad} is the radiation temperature.

With this approximation we obtain the following expression for the ionisation rate,

$$R_{12} = \frac{8\pi}{c^2}\ \alpha_0 \nu_0^3 \int_{\nu_0}^{\infty} \frac{1}{\nu} \frac{1}{e^{h\nu/kT_{rad}} - 1} d\nu. \tag{2.11}$$

Now, the integral in equation 2.11 may be rewritten using *the first exponential integral* function, $E_1(t)$. By letting $x_0 = h\nu_0/kT_{rad}$ we get

$$R_{12} = \frac{8\pi}{c^2}\ \alpha_0\ \nu_0^3\ E_1(x_0)\ , \tag{2.12}$$

where

$$E_1(x_0) = \int_1^{\infty} \frac{e^{-x_0\ x}}{x}\ dx. \tag{2.13}$$

We use the threshold ionisation frequency ν_0 and the threshold photoionisation cross section α_0 of Vernazza et al. (1981),

$$\nu_0 = 3.29 \times 10^{15}\ \text{Hz} \quad \alpha_0 = 6.32 \times 10^{-22}\ \text{m}^2\ . \tag{2.14}$$

As long as T_{rad} is not higher than 1.5×10^4K, then $x_0 > 10$ and we can use the asymptotic value of $E_1(x)$ (Abramowitz and Stegun, 1964) given by

$$E_1(x) = \frac{e^{-x}}{x}\left[1 - \frac{1}{x} + \frac{2}{x^2}\right]. \tag{2.15}$$

Finally, taking into account that the gas we study is ionised by radiation coming from one hemisphere of the sun, the ionisation rate in equation 2.11 has to be divided by two, and the ionisation rate is then

$$R_{12} = \frac{4\pi}{c^2}\ \alpha_0\ \nu_0^3\ \frac{e^{-x_0}}{x_0}\ , \tag{2.16}$$

in units s^{-1}. We also study the ionisation of hydrogen due to radiation from the corona, but in this case, for simplicity, we only adjust the ionisation rate in equation 2.16 by using different values for T_{rad} in x_0 (see table 4.1).

2.1.2 Collisional ionisation

There are several different ionisation mechanisms due to collisions. We only consider *direct ionisation* in this work. Direct ionisation happens when an atom collides with an electron producing two electrons and a singly ionised atom. The direct ionisation rates for the elements H, O, Ne, Mg and Si are taken from Arnaud and Rothenflug (1985), while the direct ionisation rate

for iron is taken from Arnaud and Raymond (1992). The rate coefficient for direct ionisation can be written

$$c_{DI}(T) = 6.69 \cdot 10^{-13} \ \left(\frac{e}{kT}\right)^{3/2} \ \frac{\exp(-x)}{x} F(x) \ , \tag{2.17}$$

in units of $\mathrm{m}^3\ \mathrm{s}^{-1}$, where

$$x = \frac{eI}{kT} \tag{2.18}$$

$$F(x) = A\ (1 - x\ f_1(x)) \ + B\ (1 + x - x(2+x) f_1(x)) + C\ f_1(x) + D\ x\ f_2(x) \tag{2.19}$$

$$f_1(x) = e^x \int_1^\infty \frac{dt}{t} e^{-tx} \tag{2.20}$$

$$f_2(x) = e^x \int_1^\infty \frac{dt}{t} e^{-tx}\ \ln(t) \ . \tag{2.21}$$

I is the first ionisation potential in units V, e is the elementary charge and A, B, C and D are fitting coefficients given in table 2.1. The integral $f_1(x)$ is evaluated using the *Hastings polynomial approximation*,

$$x\ f_1(x) = x\ e^x \int_1^\infty \frac{dt}{t} e^{-tx} = \frac{x^4 + a_1 x^3 + a_2 x^2 + a_3 x + a_4}{x^4 + b_1 x^3 + b_2 x^2 + b_3 x + b_4} + \epsilon(x) \ , \tag{2.22}$$

(Abramowitz and Stegun, 1964), where $|\epsilon(x)| < 2 \times 10^{-3}$ and

$$a_1 = 8.573328740 \quad b_1 = 9.573322345 \tag{2.23}$$

$$a_2 = 18.05901697 \quad b_2 = 25.63295615 \tag{2.24}$$

$$a_3 = 8.634760893 \quad b_3 = 21.09965308 \tag{2.25}$$

$$a_4 = 0.267773734 \quad b_4 = 3.958496923 \ . \tag{2.26}$$

$f_2(x)$ is evaluated following Hummer (1983), and the final ionisation rate C_{12} defined in chapter 2 is given by

$$C_{12} = c_{DI}\ n_p \ , \tag{2.27}$$

in units s^{-1}.

2.2 Recombination rates

The recombination rate P_{21} of the minor constituents can be written as the sum of the radiative recombination R_{21} and the dielectronic recombination

D_{21}. The radiative recombination is a form of spontaneous emission. The dielectronic recombination is a process where an unbound electron binds to the recombining ion giving its energy to the atom by exciting one of its other electrons. The excited atom deexcitates by emitting a photon. For hydrogen we obviously only have radiative recombination.

2.2.1 Radiative recombination for hydrogen

The radiative recombination rate coefficient for hydrogen is given by

$$\alpha_r(T) = 5.197 \times 10^{-20}\ \lambda^{1/2}\ \left(0.4288 + 0.5\ \ln(\lambda) + 0.469\ \lambda^{-1/3}\ \right)\ , \quad (2.28)$$

(Arnaud and Rothenflug, 1985), in units $\mathrm{m}^3\ \mathrm{s}^{-1}$, where $\lambda = 157890/T$ and T is given in K. In order to get the rate R_{ij} measured in s^{-1}, as defined in chapter 2, $\alpha_r(T)$ has to be multiplied by the electron number density, which in our model is the same as the proton number density,

$$P_{21} = R_{21} = \alpha_r\ n_p. \quad (2.29)$$

2.2.2 Recombination rates for the minor constituents

The equation for the radiative recombination rate coefficient in units $\mathrm{m}^3\ \mathrm{s}^{-1}$ (Shull and van Steenberg, 1982) is the same for all the minor constituents,

$$\alpha_r(T) = A_{rad}\ \left(\frac{T}{10^4\mathrm{K}}\right)^{X_{rad}}\ . \quad (2.30)$$

The fitting coefficients, A_{rad} and X_{rad}, are given in table 2.2. Also the dielectronic recombination rate coefficient, in units $\mathrm{m}^3\ \mathrm{s}^{-1}$ (Shull and van Steenberg, 1982), is the same for O, Ne, Mg and Si,

$$\alpha_d(T) = A_{di}\ T^{-\frac{3}{2}}\ \exp\left(-\frac{T_0}{T}\right)\ \left(1 + B_{di}\ \exp\left(-\frac{T_1}{T}\right)\right)\ . \quad (2.31)$$

The fitting coefficients A_{di}, B_{di}, T_0 and T_1 are given in table 2.2. As for hydrogen, these rate coefficients have to be multiplied with the electron (proton) density in order to get the recombination rate P_{21} in units of s^{-1},

$$P_{21} = R_{21} + D_{21} = (\alpha_r + \alpha_d)\ n_p. \quad (2.32)$$

2.2.3 Dielectronic recombination rate for iron

The equation for the dielectronic recombination rate for iron (Arnaud and Raymond, 1992) is given by

$$\alpha_d(T) = T^{-\frac{3}{2}} \sum_j c_j \exp\left(-\frac{E_j\ e}{kT}\right) , \tag{2.33}$$

in units $\mathrm{m^3\ s^{-1}}$. E_j and c_j are given by

$$E_1 = 5.12 \text{ eV} \quad c_1 = 2.2 \times 10^{-10}\ \mathrm{m^3\ s^{-1}\ K^{3/2}} \tag{2.34}$$

$$E_2 = 12.9 \text{ eV} \quad c_2 = 1.0 \times 10^{-10}\ \mathrm{m^3\ s^{-1}\ K^{3/2}} . \tag{2.35}$$

2.3 Charge transfer

The charge transfer ionisation and charge transfer recombination are, in a first approximation, the predominant transition processes for oxygen. In the charge transfer ionisation an electron jumps from a neutral oxygen to a proton resulting in a ionised oxygen and neutral hydrogen atom. Vice versa, in charge transfer recombination, an ionised oxygen and a neutral hydrogen meet to form neutral oxygen and a proton. Treating this process as a normal transition between neutral and ionised oxygen the transition rates are given by

$$P_{12} = n_p\ C_{ION} \tag{2.36}$$

$$P_{21} = n_H\ C_{REC} \tag{2.37}$$

in units $\mathrm{s^{-1}}$, where n_p and n_H is the proton and the neutral hydrogen number density, respectively. The rate coefficients C_{ION} and C_{REC} are given by

$$C_{ION} = 0.91 \times 10^{-15} \exp\left(\frac{-19.6 \times 10^{-3}\ \mathrm{V}}{kT} e\right)\left(1 - 0.93\ \exp\left(-\frac{T}{10^3 \mathrm{K}}\right)\right) \tag{2.38}$$

$$C_{REC} = 10^{-15}\left(1 - 0.66\ \exp\left(-9.3\frac{T}{10^4 \mathrm{K}}\right)\right) , \tag{2.39}$$

in units $\mathrm{m^3\ s^{-1}}$ (Arnaud and Rothenflug, 1985).

Element	I	A	B	C	D
O	13.6	9.5	-17.5	12.5	-19.5
Ne	21.6	40.0	-42.0	18.0	-56.0
Mg	7.6	18.0	-1.0	0.6	-4.0
Si	8.1	74.5	-49.4	1.3	-54.6
Fe	7.9	31.9	-15.0	0.32	-28.1

Table 2.1: Fitting coefficients for the direct ionisation rates.

	A_{rad} (m^3 s^{-1})	X_{rad}	A_{di} (m^3 s^{-1} $K^{3/2}$)	B_{di}	T_0 (K)	T_1 (K)
O	3.10(-19)	6.78(-1)	1.11(-9)	9.25(-2)	1.75(5)	1.45(5)
Ne	2.20(-19)	7.59(-1)	9.77(-10)	7.30(-2)	3.11(5)	2.06(5)
Mg	1.40(-19)	8.55(-1)	4.49(-10)	2.10(-2)	5.01(4)	2.81(4)
Si	5.90(-19)	6.01(-1)	1.10(-9)	0.0	7.7(4)	0.0
Fe	1.42(-19)	8.91(-1)	-	-	-	-

Table 2.2: Fitting coefficients for the recombination rates. $3.10(-19)$ means 3.10×10^{-19}.

2.4 Electric field

To obtain a simple expression for the electric field we write the momentum equation for the electrons,

$$\frac{\partial(n_e u_e)}{\partial t} + \frac{\partial}{\partial z}(n_e u_e u_e) = -\frac{1}{m_e}\frac{\partial}{\partial z}(n_e kT) + g n_e - \frac{n_e e}{m_e} E \ , \tag{2.40}$$

where m_e is the electron mass, n_e is the electron number density, u_e is the velocity of the electrons. Since the electron mass m_e is much smaller than every other variable, we can neglect all the terms that are not divided by m_e, and equation 2.40 becomes

$$-\frac{\partial}{\partial z}(n_e kT) = n_e \ e \ E \ . \tag{2.41}$$

We have assumed that the sun's atmosphere is quasi neutral, and hence $n_e = n_p$. Substituting this in equation 2.41 we obtain

$$-\frac{\partial}{\partial z}(n_p kT) = n_p \ e \ E \ , \tag{2.42}$$

which yields the following expression for the electric field,

$$E = -\frac{1}{e \ n_p}\frac{\partial}{\partial z}(n_p kT) \ . \tag{2.43}$$

Element	$r_{nH}(10^{-10}\mathrm{m})$
Oxygen	2.26
Neon	1.75
Silicon	2.91
Magnesium	3.09
Iron	3.09

Table 2.3: Atomic radius for the rigid sphere approximation, taken from Marsch et al. (1995).

2.5 Collisions

The collision processes describe how the minor constituents interact with the hydrogen background. In this section we will treat three different collision processes. Neutral-neutral collisions (collisions between neutral minor constituents and neutral hydrogen), neutral-ion collisions (both collisions between neutral minor constituents and protons, and collisions between neutral hydrogen and ionised minor constituents), and finally the very important collisions between ionised particles (protons and ionised minor constituents). Collisions between two minor constituents are neglected.

Proton-ion collisions are the absolutely strongest ones. Their rate coefficients are at least two (often three) orders of magnitude stronger than the rate coefficients for neutral-ion and neutral-neutral collisions. Neutral-neutral and neutral-ion collisions have rate coefficients of the same order of magnitude.

2.5.1 Neutral-neutral collisions

When describing the collisions between neutral particles we use the so called *rigid sphere approximation*. The collision frequency for neutral-neutral collisions (Banks and Kockarts, 1973) (Schunk, 1977) is given by

$$\nu_{12} = \frac{4}{3}\frac{m_2}{m_1 + m_2}\, n_2\, \sigma_0\, v_{12}\ , \tag{2.44}$$

in units s^{-1}, where m_1 and m_2 are the masses of the colliding particles, v_{12} is the relative velocity, n_2 is the number density of the neutral hydrogen gas, and $\sigma_0 = \pi r_{nH}^2$ is the collision cross section. The values of r_{nH} for the different minor constituents (Marsch et al., 1995) are given in table 2.3. Assuming thermal and dynamic equilibrium, the distribution of the velocities is given by the Maxwell distribution and the average relative speed between

Element	α
Hydrogen	0.74
Oxygen	0.88
Iron	9.3
Neon	0.44
Silicon	6.0
Magnesium	11.8

Table 2.4: Neutral gas atomic polarizability. $[\alpha] = 10^{-40}$ C^2 s^2 kg^{-1}

the particles is

$$v_{12} = \left(\frac{8\ k}{\pi}\ \frac{T}{\mu} \right)^{\frac{1}{2}} \ , \tag{2.45}$$

where the reduced mass μ is given by

$$\mu = \frac{m_1\ m_2}{m_1 + m_2}. \tag{2.46}$$

Equation 2.44 and 2.45 yields the following expression for the collision frequency,

$$\nu_{12} = \frac{4}{3}\ \frac{m_2}{m_1 + m_2}\ n_2\ \sigma_0 \left(\frac{8\ k}{\pi}\ \frac{T}{\mu} \right)^{\frac{1}{2}} . \tag{2.47}$$

2.5.2 Neutral-ion collisions

In a neutral-ion collision the most important interaction is represented by an induced dipole attraction. The average collision rate (Schunk, 1977), in units s^{-1}, is given by

$$\nu_{12} = \frac{4}{3}\ \frac{m_2}{m_1 + m_2}\ n_2\ v_{12}\ Q_D. \tag{2.48}$$

n_2 is now or the neutral or the ionised hydrogen number density, and Q_D is the average momentum transfer cross section for collisions between ions and neutral particles, given by

$$Q_D = 0.260 \left(\frac{\alpha}{kT} \right)^{\frac{1}{2}} \frac{e}{\epsilon_0} \ , \tag{2.49}$$

where α is the neutral gas atomic polarizability and ϵ_0 is the permittivity of vacuum. The polarizabilities α for the different elements (Marsch et al., 1995) are given in table 2.4. The average relative speed is given by the same

formula as for collisions between neutral particles (see equation 2.45), and with the expression for the cross section in equation 2.49, equation 2.48 can be written as

$$\nu_{12} = 0.553 \ \frac{m_2}{m_1 + m_2} \ n_2 \left(\frac{\alpha}{\mu}\right)^{\frac{1}{2}} \frac{e}{\epsilon_0}. \tag{2.50}$$

2.5.3 Ion-ion collisions

Collisions between charged particles are described by the so called *Coulomb interaction*. The collision frequency for such collisions (Schunk, 1977), in units s^{-1}, is given by

$$\nu_{12} = \frac{1}{3 \ \epsilon_0^2} \ \frac{n_2 \ m_2}{m_1 + m_2} \left(\frac{2\pi kT}{\mu_{12}}\right)^{-\frac{3}{2}} \ \frac{e_1^2 \ e_2^2}{\mu_{12}^2} \ \ln\Lambda \ , \tag{2.51}$$

where the electric charge e_1 and e_2 of the two particles are, in our case, both equal the elementary charge e. This is because we only treat singly ionised ions. The *Coulomb logarithm*, $\ln\Lambda$, is given by

$$\Lambda = 24\pi \ n_e \ L_D^3 \ , \tag{2.52}$$

where L_D is the Debye length, that for a pure hydrogen plasma is given by

$$L_D = \left(\frac{4\pi}{kT} \ \frac{e^2}{4\pi\epsilon_0} \ (n_e + n_p)\right)^{-\frac{1}{2}} \ . \tag{2.53}$$

Since we study a quasi neutral atmosphere, i.e. $n_e = n_p$, equation 2.53 may be written as

$$L_D = \sqrt{\frac{kT\epsilon_0}{2e^2 n_p}} \ . \tag{2.54}$$

Finally we obtain the following expression for the Coulomb logarithm,

$$\ln\Lambda = \ln\left(\frac{24\pi n_p}{e^3} \left(\frac{kT\epsilon_0}{2n_p}\right)^{\frac{3}{2}}\right). \tag{2.55}$$

Chapter 3

The numerical model

3.1 Double grid

The model describes a slab of the solar atmosphere of a given thickness. The slab is divided into cells, where every cell is characterised by a lower border, an upper border and a centre. Some physical quantities are defined in the cell's centre while others are defined on the cell's borders. This is why the system is called a "double grid": the cells' borders constitute a first grid, *the border grid*, and the cells' centres define a second grid, *the centre grid*. The gas velocity and the mass flux are defined on the border grid, while the gas densities and the gas temperature are defined on the centre grid.

Going into details, we define a velocity u_j that describes the gas velocity on the j-th border and a density n_j that gives the gas density in the centre of the j-th cell, where j is the spatial discretisation index. As one can see from Fig. 3.1 the j-th cell is delimited between the borders labelled as j and $j+1$. Then the j-th border is the limit between the j-th and the $j-1$-th cell.

Like the velocity, the mass flux, given by $n\ u$, is also calculated on the border and we therefore need an estimate of the density on the border, called $\hat{n}_j$. In the code, two different ways to estimate the density values on the

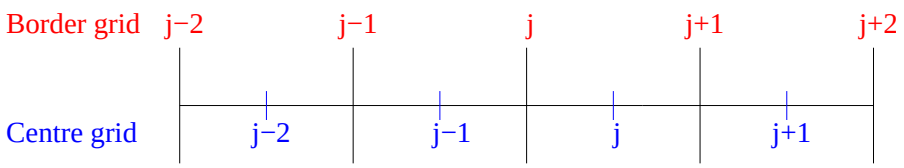

Figure 3.1: The double grid structure.

borders have been used. The first one is an easy two points average,

$$\hat{n}_j = \frac{1}{2}(n_{j-1} + n_j), \tag{3.1}$$

and the second one is a more elaborated average using a second order upwind differencing scheme to estimate an advective flux. The two points average is used in all terms of equation 2.2, except the first term on the right hand side (pressure gradient term), which has no need for any value of $\hat{n}_j$, and the second term on the left hand side (advection term), where the upwind scheme is used. The latter is also used in the second term of the left hand side of equation 2.1.

In the same way, we can define the averaged velocity of the cell centre,

$$\hat{u}_j = \frac{1}{2}(u_j + u_{j+1}), \tag{3.2}$$

but this time only the two points average has been used.

3.2 Semi-implicit scheme

The aim of the code is to integrate the continuity and the momentum equations (equation 2.1 and 2.2) in time. The scheme used to solve these equations is a semi-implicit scheme, which means that it is a mix of an explicit and an implicit scheme.

In the explicit part every unknown variable is a function of known variables only. To exemplify we consider the quantity $q(p, r)$, which is a function of the quantities p and r. In an explicit scheme at a certain time step $i + 1$, the quantity q is only a function of p and r at previous time steps, $q^{i+1} = q^{i+1}(p^i, r^i, p^{i-1}, ...)$. The explicit scheme for the left hand side of the continuity equation is given by

$$\frac{n_j^{i+1} - n_j^i}{\Delta t} + \frac{\left(\hat{n}_{j+1}^i \; u_{j+1}^i - \hat{n}_j^i \; u_j^i\right)}{\Delta z} \; . \tag{3.3}$$

Thus, the explicit scheme provides an easy way to determine numerically the evolution of the physical quantities when the values at the previous time step are known. Unfortunately, explicit methods are characterised by unstable solutions. These can be studied introducing the Courant-Friedrichs-Lewy stability criterion (Press et al., 1992), which sets a lower limit for the ratio between spatial increment Δz and time step Δt.

The code is used to find both time dependent and steady state solutions, which requires big time steps. It is therefore preferable to avoid any upper

limit for the time step Δt. In order to avoid this, we need to use an implicit scheme.

In implicit schemes, the quantity q^{i+1} is coupled with all the other quantities at the same time step, $q^{i+1} = q(p^{i+1}, r^{i+1}, p^i, r^i, ...)$. It is therefore no longer possible to calculate explicitly every quantity one by one. Hence, the whole system of coupled equations needs to be solved for each time step t_i. The implicit scheme for the left hand side of the continuity equation becomes

$$\frac{n_j^{i+1} - n_j^i}{\Delta t} + \frac{\left(\hat{n}_{j+1}^{i+1}\ u_{j+1}^{i+1} - \hat{n}_j^{i+1}\ u_j^{i+1}\right)}{\Delta z}\ . \tag{3.4}$$

Since all the quantities are coupled in the implicit scheme, there is no upper limit for time step Δt. In our code implicit and explicit parts are mixed, i.e. the variables in the advective term of the continuity equation (2.1) and the momentum equation (2.2) are defined as

$$\bar{u}_j = \beta\ u_j^{i+1} + (1-\beta)\ u_j^i \tag{3.5}$$

and

$$\bar{\hat{n}}_j = \beta\ \hat{n}_j^{i+1} + (1-\beta)\ \hat{n}_j^i, \tag{3.6}$$

where β determines how implicit the code is. $\beta = 0$ gives a fully explicit code, $\beta = 1$ gives a fully implicit code, and any number between 0 and 1 makes the code semi-implicit.

By defining the cell volume $\Delta V = A\Delta z$, where A is the unit surface, equation 3.3 can be written as

$$\Delta V\left(n_j^{i+1} - n_j^i\right) + A\Delta t\left(\bar{\hat{n}}_{j+1}\ \bar{u}_{j+1} - \bar{\hat{n}}_j\ \bar{u}_j\right) = 0. \tag{3.7}$$

The discretisation of the right hand side of the continuity equation (equation 2.1) proceeds similarly, with the only note that we choose to write the ionisation term as a fully implicit - and not semi-implicit - term.

Also the discretisation of the momentum equation follows the same steps, and the explicit expression for the left hand side of equation 2.2 is,

$$\begin{aligned}&\frac{\hat{n}_j^{i+1}u_j^{i+1} - \hat{n}_j^i u_j^i}{\Delta t} + \\ &\frac{\left(\hat{n}_{j+1}^i u_{j+1}^i + \hat{n}_j^i u_j^i\right)\hat{u}_j^i - \left(\hat{n}_j^i u_j^i + \hat{n}_{j-1}^i u_{j-1}^i\right)\hat{u}_{j-1}^i}{\Delta z}\ .\end{aligned} \tag{3.8}$$

A combination of equation 3.8 and the corresponding implicit scheme gives the semi-implicit expression

$$\begin{aligned}\Delta V\left(\hat{n}_j^{i+1}u_j^{i+1} - \hat{n}_j^i u_j^i\right) + A\Delta t\left(\bar{\hat{n}}_{j+1}\bar{u}_{j+1} + \bar{\hat{n}}_j\bar{u}_j\right)\bar{\hat{u}}_j \\ - \left(\bar{\hat{n}}_j\bar{u}_j + \bar{\hat{n}}_{j-1}\bar{u}_{j-1}\right)\bar{\hat{u}}_{j-1}\ ,\end{aligned} \tag{3.9}$$

where we have defined

$$\bar{\hat{u}}_j = \beta\ \bar{u}_j^{i+1} + (1-\beta)\ \bar{u}_j^i\ . \tag{3.10}$$

Without going into details, we will describe how the different terms on the right hand side of the momentum equation (2.2) can be implemented in a discretised scheme, by specifying if the implicit or semi-implicit form is used. The *pressure gradient* term contains semi-implicit centre-grid values of the density, defined similarly to equation 3.6. The *electric field* term is equal to the pressure gradient term in the hydrogen background, which means that it contains semi-implicit centre-grid values of the (proton) density. In the code for the minor constituents the electric field depends on the fully implicit minor constituent density value at the cell borders, and on the time-independent proton pressure also evaluated at the cell borders. The *gravity* term depends on the semi-implicit border-grid values of the density. The *ionisation*, the *charge transfer* and the *collision* terms are calculated from fully implicit border-grid values of the density and the velocity.

3.3 Newton-Raphson method

As we have seen in section 3.2, a semi-implicit scheme leads to a system of coupled nonlinear equations that we want to solve with respect to n^{i+1} and u^{i+1} for every time step i. In order to do this, the Newton-Raphson method is applied (Press et al., 1992). As a first step, we define a vector E_j that contains all the discretised system equations, both for the continuity and for the momentum equation. These equations have a component for every cell j.

The solution for the $i+1$ time step yields the value n^{i+1} and u^{i+1} for which

$$E_j(n_k^{i+1}, u_k^{i+1}, n_{k-1}^{i+1}, \ldots) = E_j(x_k^{i+1}, \ldots) = 0, \tag{3.11}$$

where x_k^i is a vector of components n_k^i, u_k^i, and k is a second space index. We write x_k^{i+1} as the sum of the previous value x_k^i and a correction Δx_k^i,

$$x_k^{i+1} = x_k^i + \Delta x_k^i, \tag{3.12}$$

where Δx_k^i is the unknown variable. If the time step is small enough, we assume that also the corrections are small,

$$\frac{|\Delta x_k^i|}{x_k^i} \ll 1. \tag{3.13}$$

With this assumption it is possible to linearise the solution, neglecting the higher order terms in $\frac{|\Delta x|}{x}$, e.g.,

$$x_k^{i+1} \cdot x_k^{i+1} \approx x_k^i \cdot x_k^i + 2x_k^i \Delta x_k^i + \text{higher orders.} \tag{3.14}$$

Let us assume that we do not know the real solutions x_k^{i+1}, but only their estimate x_k^t, called test solution. Then the vector $\underline{E}$ is no longer zero, but quantifies the error from the estimate. The aim of the Newton-Raphson method is to find the right correction that nullifies the error, or at least makes it negligible. The steps of the Newton-Raphson method are given by

$$E_j(x_k^t) \neq 0, \tag{3.15}$$

$$E_j(x_k^t + \Delta x_k) = 0. \tag{3.16}$$

Assuming again that the correction is small, $\frac{|\Delta x_k|}{x_k^t} \ll 1$, we can rewrite E_j as a Taylor series

$$E_j(x_k^t + \Delta x_k) \approx E_j(x_k^t) + \sum_k \frac{\partial E_j}{\partial x_k}\Big|_{x_k = x_k^t} \Delta x_k = 0. \tag{3.17}$$

By defining a new operator W_{jk} as

$$W_{jk} = -\frac{\partial E_j}{\partial x_k}, \tag{3.18}$$

we can rewrite equation 3.17 as

$$E_j(x_k^t + \Delta x_k) \approx E_j(x_k^t) - \sum_i W_{jk}(x_k^t)\Delta x_k = 0, \tag{3.19}$$

or in matrix form

$$\mathbf{W} \cdot \underline{\Delta x} = \underline{E}(\underline{x}^t). \tag{3.20}$$

If we invert the matrix W, we get

$$\Delta \underline{x} = \mathbf{W}^{-1} \underline{E}(\underline{x}^t), \tag{3.21}$$

that allows us to calculate a new value of $\underline{x}$,

$$\underline{x}^{t'} = \underline{x}^t + \Delta \underline{x}. \tag{3.22}$$

The partial derivatives that constitute the matrix element W_{jk} are different from zero only when $j - 2 \leq k \leq j + 2$, because of the second order

upwind scheme used in the advective term. This results in a pentadiagonal matrix, with big simplifications concerning the matrix inversion.

The Newton-Raphson method gives exact result when the system is made up of linear equations. This is not the case here, because in the Taylor expansion we have neglected all the higher order terms including the second order. However, if the test solution is not too far from the real solution, i.e. $\frac{|\Delta x|}{x} \ll 1$, hopefully the new solution obtained with the Newton-Raphson method can bring us closer to the right solution. If this is the case, we can solve the system with an iterative procedure, otherwise, if the new solution is not converging, it is necessary to repeat the whole process with a smaller time step Δt.

3.4 Boundary conditions

In this section we will describe the role of the boundary conditions, and how they are implemented. The physical values of the boundary conditions are not the same for the background and the minor constituents, and also vary between the different background models. They are therefore given for each specific case in later sections.

The boundary conditions are very important because they describe the physical system outside the grid and constitute the way to communicate all the necessary external conditions to the modelled layer. For example it is through the boundary conditions that we simulate the presence of the atmosphere below the lower boundary, avoiding in this way the whole atmosphere to fall in a gravitational collapse.

The boundary conditions supply the values for the border density $\hat{n}$ (see section 3.1) and the border velocity u on the left border of the first cell and on the last cell's right border.

It is important to differentiate the *fixed* and the *floating* boundary conditions. While a fixed boundary forces the boundary to have a determined value, the floating condition allows the boundary to just follow the same behaviour as the nearby grid points. A typical example of a floating boundary equation is the flux conservation, where the particle flux is conserved from the first grid point to the second.

Specifying a fixed density value simulates a rigid wall at the beginning or end of the grid, and can often cause reflection problems. In order to give information about the physical system without building a reflective wall we use the method of characteristics described by Korevaar and van Leer (1988).

The main idea is to build a boundary condition that has a non-reflective behaviour but is still carrying information from the system outside the grid.

This is achieved by a set of equations that permits the boundary to oscillate around a fixed value, in order for the perturbations to pass through it.

Lower boundary This method considers a undisturbed hydrogen gas at the lower boundary (where $z = z_0$) which has fixed values for the density and velocity, n_o and u_o, respectively. The true boundary value n_l and u_l are calculated by a sort of interpolation between the undisturbed values n_o and u_o and the densities and velocities at the first and the second grid pointn_1, u_1, n_2 and u_2. The boundary condition for the density is then given by

$$n_l = \frac{1}{kT_0} exp\left(\frac{\gamma(a_l + u_0 - u_1) + c_0 \log(n_0 kT_0) + c_1 \log(n_1 kT_1)}{c_0 + c_1}\right) \tag{3.23}$$

where $c_o = \sqrt{\frac{kT_0}{m_H}}$ is the sound speed of a pure hydrogen gas at temperature T_0, and m_H is the hydrogen mass. γ is the heat capacity ratio, and the parameter a_l is given by

$$a_l = \frac{z_1 - z_0}{z_2 - z_1}\left[\frac{c_2}{\gamma}\log\left(\frac{n_1 T_1}{n_2 T_2}\right) - (u_1 - u_2)\right]. \tag{3.24}$$

where c_i, T_i, and z_i are the sound speed, the temperature and the height for the first ($i = 1$) and the second ($i = 2$) grid point. The boundary condition for the velocity is given by

$$u_l = u_0 - \frac{c_0}{\gamma}\log\left(\frac{n_l}{n_0}\right). \tag{3.25}$$

Upper boundary The conditions for the upper boundary follow the same principles as for the lower boundary. The undisturbed values n_0, u_0 and n_{TOP}, u_{TOP} are specified in the different cases presented later.

Chapter 4

Results

4.1 Background

The results obtained vary strongly depending on the ionisation degree of the minor constituents and the ionisation degree of the background. We therefore study the behaviour of the minor constituents in four different hydrogen backgrounds, labelled A - D. The first one, model A, is almost neutral, model B is approximately 5% ionised, model C is approximately 50% ionised, and model D is almost fully ionised. The chosen values of the parameter T_{rad} for each model are given in table 4.1 together with the photoionisation rates (which depend on T_{rad}) and the final ionisation degrees of the different models.

In model A the radiative ionisation rate for hydrogen is only one order of magnitude greater than the collisional ionisation rate, and both rates therefore influence the ionisation degree of the background. In model B the radiative ionisation rate is increased, being now two orders of magnitude greater than the collisional ionisation rate, and the latter one does therefore not alter the ionisation degree of the background significantly. In model C and D the radiative ionisation rates are increased additionally, and hence the collisional ionisation is also here negligible for hydrogen.

Model	T_{rad} (K)	R_{12} (s^{-1})	Ionisation degree
A	5000	1.9×10^{-6}	0.4% - 1.2%
B	5780	1.5×10^{-4}	3.6% - 9.0%
C	7000	2.2×10^{-2}	31% - 57%
D	7500	4.1×10^{-1}	61% - 84%

Table 4.1: Ionisation parameters for the four background models.

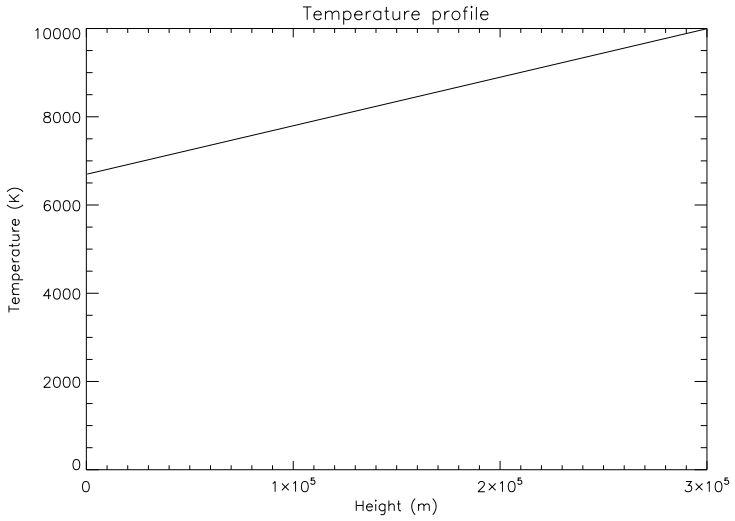

Figure 4.1: The temperature profile in all four background models.

Since we do not solve the energy equation, the temperature profile that we use as an input for all four background models, is constant in time. Figure 4.1 shows that this temperature increases linearly from 6700K at the lower boundary to 10000K at the upper boundary. The height z of the slab is 3×10^5m, which corresponds to approximately one hydrogen scale height at 10^4K. We have fixed the total hydrogen density at the lower boundary at 2×10^{17} m^{-3}, while the total hydrogen flux at the upper boundary is fixed to zero. The initial neutral hydrogen density is given by its *hydrostatic equilibrium density*, and the initial ionisation degree is between 1% and 2%. For a deeper discussion of the boundary conditions, see section 3.4. There is hydrostatic equilibrium if only the two first terms (pressure gradient and gravity) on the right hand side of equation 2.3 and 2.4 are different from zero (when both terms on the left hand side are zero),

$$\frac{1}{1+q_i}\frac{1}{m}\frac{\partial}{\partial z}(nkT) = gn, \tag{4.1}$$

where g is negative, and the factor $\frac{1}{1+q_i}$ takes into account the fact that the proton pressure is twice the neutral hydrogen pressure due to the electric field (see section 2.4); $q_1 = 0$ and $q_2 = 1$. If we integrate this expression with respect to z, we get the hydrostatic equilibrium density as a function

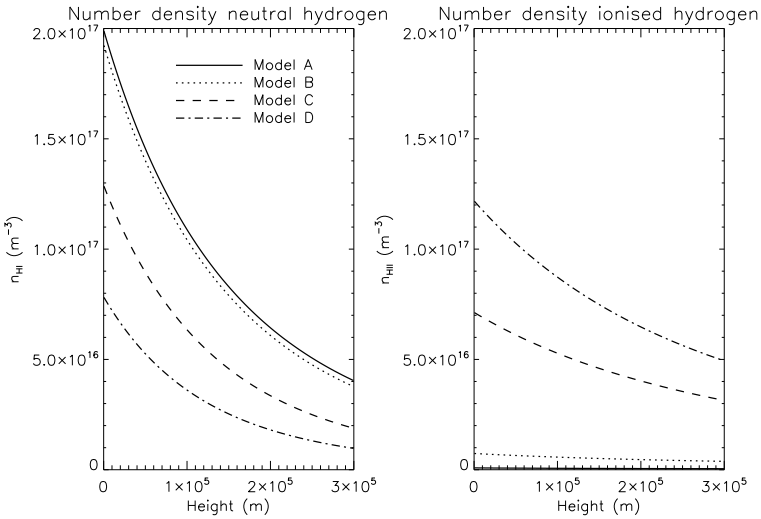

Figure 4.2: The neutral hydrogen and proton number densities. The proton density in model A is small compared to the other models, hence the full line in the right panel is not visible.

of height,

$$n_i(z) = n_{i0}\ \frac{T_0}{T}\ \exp\left(\frac{1}{1+q_i}\frac{mg}{k}\int\frac{1}{T}dz\right)\ , \tag{4.2}$$

where n_{i0} and T_0 are the lower boundary values of the density and the temperature respectively. Index $i = 1$ represents neutral hydrogen and $i = 2$ protons.

The code is run until steady state is reached for each model. Model A needs the longest run time, $\sim 2\times10^4$s, and model D the shortest, $\sim 1\times10^3$s. This difference is due to the different ionisation and recombination rates. From the ionisation rates in table 4.1 one could expect the run time for model A to be about $10^5 - 10^6$s, and for model D only a few seconds. Since we start with more than 1% ionisation over the whole layer and end up with less than 1% for most of the layer in model A, it is the recombination rate that determines the run time in this model. The recombination rate vary with time because it depends on the electron (proton) density, but it is of magnitude 10^{-4} s^{-1}, and hence it is sufficient to run the code for 2×10^4s. With model D a 40% ionisation is obtained during the first five seconds. After fifty seconds model D is very close to the final ionisation degree, but the neutral hydrogen and proton densities oscillate at the upper boundary and the code needs a long time to stabilise. The final steady state number

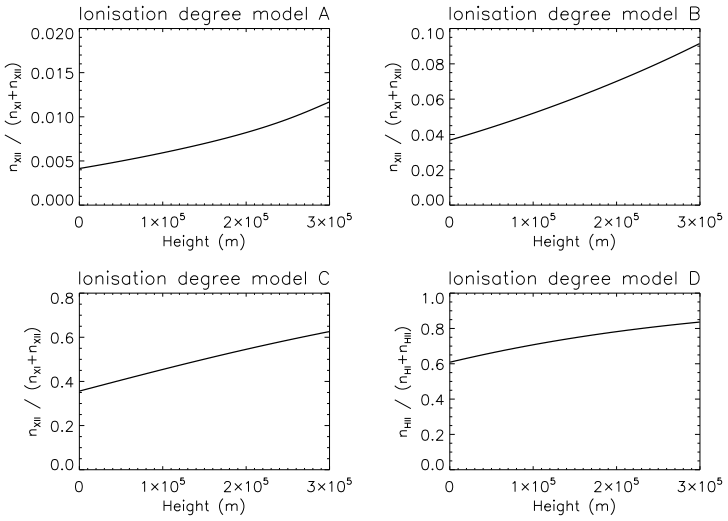

Figure 4.3: The ionisation degrees in the four background models. The photoionisation rate is increased from model A to D.

densities and velocities are used as background when we solve for the minor constituents.

The neutral and ionised hydrogen number densities in the four models are compared in figure 4.2. The proton number density in model A is approximately zero. The ionisation degrees in the four models are shown in figure 4.3. As already mentioned, an increasing photoionisation rate from A-D causes the increase in ionisation degree. The densities are obviously not the same in the four models, but the main features are very similar, and we will therefore in the following only discuss model B in detail.

Figure 4.4 shows the steady state neutral and ionised hydrogen densities compared to their respective hydrostatic equilibrium densities. The *hydrostatic equilibrium scale height* for protons is twice the one for neutral hydrogen due to the electric field (see equation 4.2). The neutral hydrogen density decreases slightly faster than the hydrostatic equilibrium density, while the proton density decreases much slower than the hydrostatic equilibrium density. The hydrogen velocities in steady state are shown in figure 4.5. The neutral hydrogen velocity is positive and the proton velocity is negative in all the four models. The neutral hydrogen velocity increases from model A to D, while the proton velocity is clearly reduced (in absolute value), and as required from the upper boundary condition, the total flux (neutral hydrogen flux + proton flux) is zero (see figure 4.6).

The ionisation process in the system forces the neutral hydrogen and

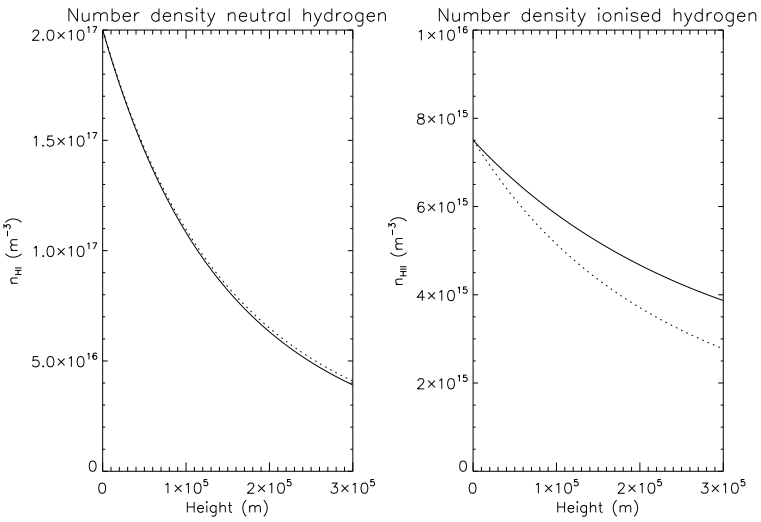

Figure 4.4: The number densities for hydrogen in model B. The solid curves are our results while the dotted curves are the hydrostatic equilibrium densities given by equation 4.2.

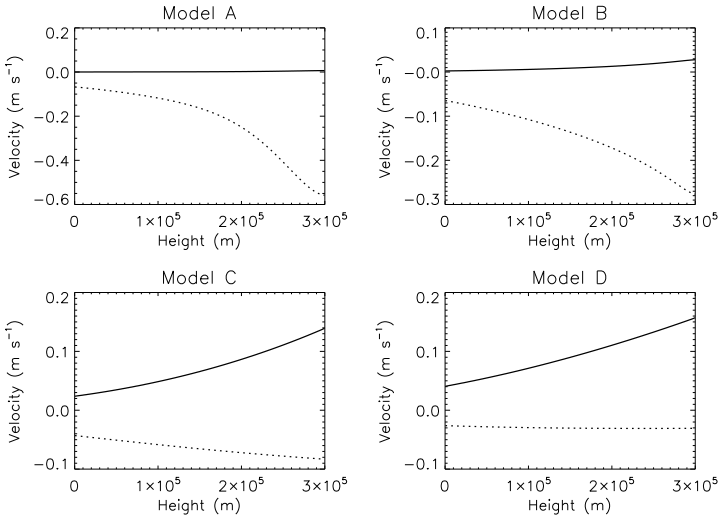

Figure 4.5: The neutral hydrogen (solid curve) and proton (dotted curve) velocities in all four background models.

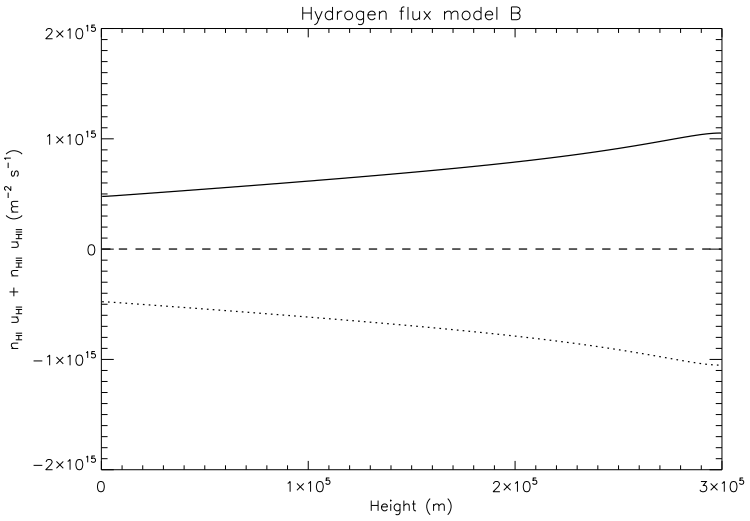

Figure 4.6: Steady state neutral hydrogen flux (solid curve), proton flux (dotted curve) and total hydrogen flux (dashed curve).

proton densities to be respectively smaller and larger than their hydrostatic equilibrium densities, and it is therefore responsible for the counter flowing neutral and ionised hydrogen gases. In order to understand the physics behind the hydrogen fluxes, the force balance in the system needs to be studied. The advection terms in equation 2.3 and 2.4 are neglected because they are small compared to the forces on the right hand side. At steady state the right hand side terms cancel, and we study which term dominates. We label the right hand side terms as follows,

$$\text{Pressure gradient} = -\frac{1+q_i}{m_i}\ \frac{1}{n_i}\ \frac{\partial}{\partial z}(n_i k T) \tag{4.3}$$

$$\text{Gravity} = g \tag{4.4}$$

$$\text{Collisions} = k_{mt}\ n_j(u_j - u_i) \tag{4.5}$$

$$\text{Ionisation/recombination} = \frac{n_j}{n_i}\ u_j\ P_{ji} - u_i\ P_{ij}\ , \tag{4.6}$$

in units m s^{-2}.

The force balance for neutral hydrogen in figure 4.7 (left panel) shows that neutral hydrogen is very close to hydrostatic equilibrium. In fact, there is almost a balance between the pressure gradient and gravity, and the contribution from the collision term is small compared to the other two. The force balance for protons in the right panel of figure 4.7, shows that the collision term is larger than the pressure gradient and the electric field taken

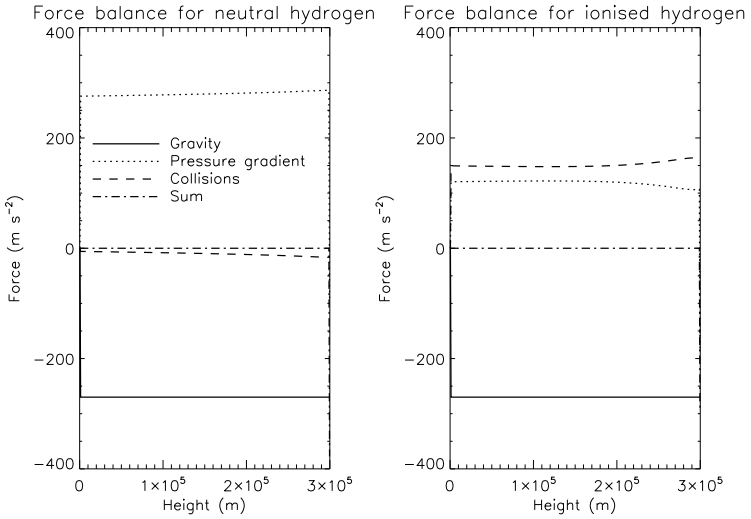

Figure 4.7: The force balance for neutral hydrogen and protons in model B. The electric field for protons is included in the pressure gradient term.

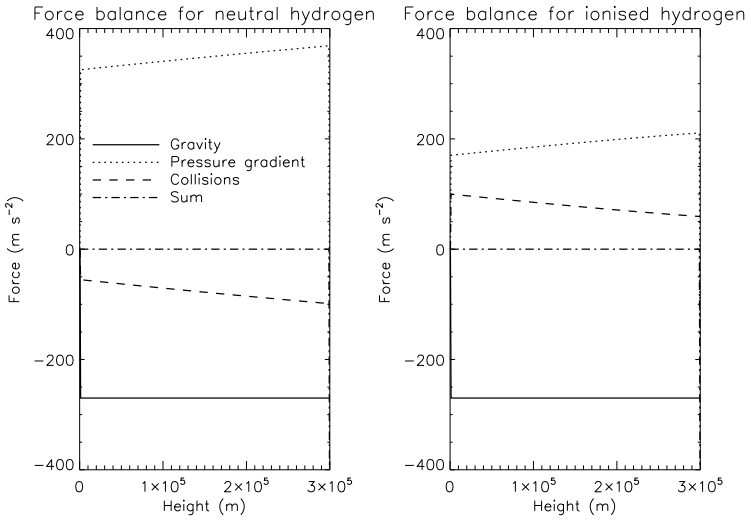

Figure 4.8: The force balance of neutral hydrogen and protons in model C. The electric field for protons is included in the pressure gradient term.

together. Hence, the protons are not close to hydrostatic equilibrium. Moreover, friction due to the ionisation/recombination process is negligible for both protons and neutral hydrogen. Since the neutral hydrogen velocity is positive and the proton velocity is negative, the collision term is negative for neutral hydrogen and positive for protons. The relation between the two collision terms is given by Newton's third law.

The collision term is proportional to the difference between the neutral hydrogen and the proton velocity, but for the protons, it is also proportional to the neutral hydrogen density. For neutral hydrogen it is proportional to the proton density. Thus, when the ionisation degree is low, as in model B, it is not surprising that the collisional interaction is more important for the protons than for the neutral hydrogen. Figure 4.8 shows that in model C, with approximately 50% ionisation, the collision term is of the same magnitude for neutral hydrogen and protons.

4.2 Minor constituents

We have set the initial value of the absolute abundance to $\mathcal{A} = 5 \times 10^{-4}$ for all the minor constituents. This is the photospheric abundance of oxygen (see table 1.1). For comparison reasons we use this value for all the minor constituents, even if they in reality have different abundances. The initial value for the ionisation degree of the minor constituents is 0.1%, and both neutral and ionised velocities are set to zero at $t = 0$. The neutral density is fixed at the lower boundary, while at the upper boundary both the neutral and the ionised velocities are fixed to zero.

The rates for the minor constituents, magnesium, silicon, neon and iron are given by radiative and dielectric recombination and by collisional ionisation, but for oxygen by charge exchange. Since both the ionisation and recombination rates are directly proportional to the electron (proton) density, the final ionisation degree of the minor constituents, except for oxygen, does not vary significantly from one model to another. The ionisation degree of oxygen is strongly related to the ionisation degree of hydrogen because of the charge exchange interaction between these elements (see section 4.2.1).

In the same way as done for the hydrogen background, we solve equation 2.1 and 2.2 for the minor constituents one by one, by running the code until steady state is reached. Steady state is reached after approximately $10^5 - 10^7$s, depending on the element in consideration.

When studying the relative abundances in the upper atmosphere, one usually compare with the corresponding photospheric abundance ratio. In this study, since all the minor constituents are equally abundant in the pho-

tosphere (first grid point), the abundances we obtain in the upper chromosphere are not the real abundances, but rather the so called FIP fractionation, defined by equation 1.3.

Since the behaviour of all the minor constituents are compared to oxygen, it is appropriate to start with a presentation of the oxygen results.

4.2.1 Oxygen

The gravitational settling of oxygen proceeds as illustrated in figure 4.9, where the absolute oxygen abundance after one, five and sixty minutes in all four background models is shown. In model A, B and C it can clearly be seen how the oxygen gas in the upper part of the atmosphere layer falls towards the sun during the first hour of gravitational settling. In model A and B the absolute oxygen abundance at the upper boundary is reduced by at least a factor of ten after one hour. In model C the reduction of the absolute oxygen abundance is slower compared to model A and B, but at the upper boundary, after one hour, the amount of oxygen compared to hydrogen is reduced by half. In model D it is hardly possible to see any oxygen reduction at all.

We define the *settling time* t_s for oxygen in each model as the time it takes before the number density, $N_{\rm O}$, is 10% of the initial number density at the upper boundary z_u,

$$\frac{N_{\rm O}(z_u, t_s)}{N_{\rm O}(z_u, t=0)} = 0.1 \ . \tag{4.7}$$

The settling times for oxygen in model A and B are similar, $t_s \simeq 2 \times 10^3$s in model A and $t_s \simeq 3 \times 10^3$s in model B. In model C the settling time is $t_s \simeq 3 \times 10^4$s and in model D $t_s \simeq 2 \times 10^5$s.

The reason why oxygen behaves differently from one model to another is because of the increase in the ionisation degree of the background which leads to an increase of the ionisation degree of oxygen. In fact, as shown in figure 4.10, the ionisation degree of oxygen is strongly related to the ionisation degree of hydrogen. By neglecting the advection term of the equation of mass conservation for oxygen (equation 2.1) (which is reasonable since it is three orders of magnitude smaller than the other terms) and by assuming that the ionisation balance is reached, the left hand side of the equation is zero, and the right hand side can be rewritten as

$$\frac{n_2}{n_1} = \frac{n_p}{n_H} \frac{C_{ION}}{C_{REC}} \ , \tag{4.8}$$

where n_1 is the neutral oxygen number density and n_2 is the ionised oxygen number density. This means that the ionisation degree of oxygen is propor-

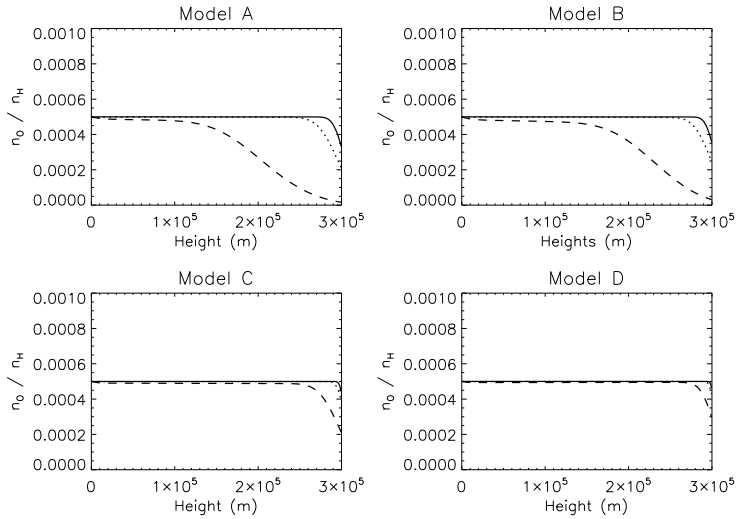

Figure 4.9: The absolute abundance of oxygen in the four background models. The solid curve is reached after one minute, the dotted curve is reached after five minutes and the dashed curve is reached after one hour.

tional to the ionisation degree of hydrogen, with proportionality constant $\frac{C_{ION}}{C_{REC}} = 0.9$.

The neutral and ionised oxygen velocities diminish during the gravitational settling. This is illustrated in figure 4.11, where the velocities for neutral and ionised oxygen in model B and C are plotted after one, five and sixty minutes. One can see from this figure that the (absolute and relative) velocity reduction is larger in model B than in model C. From the same figure it is also clear that both the neutral and the ionised oxygen velocity diminish when the background (and hence also the oxygen) ionisation degree increases from approximately 5% in model B to approximately 50% in model C.

As done for hydrogen, the force balance in the system must be studied in order to explain the velocities in figure 4.11. The force balance in model B is shown in figure 4.12 and the one for model C in figure 4.13. The right hand side terms of equation 2.2 are labelled as for hydrogen, but for oxygen the ionisation/recombination term is dominated by charge exchange with hydrogen, and the collision frequency is not the same as for hydrogen. We therefore rewrite the collision and the ionisation/recombination term (now

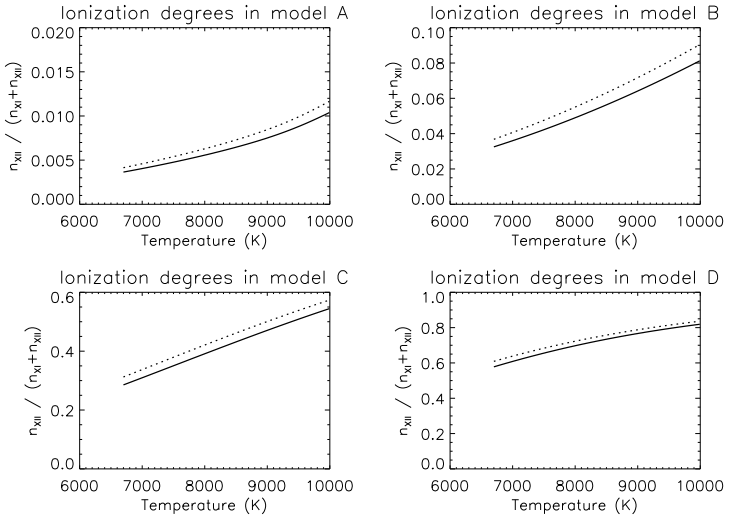

Figure 4.10: The ionisation degrees of the oxygen (solid curve) and hydrogen (dotted curve) in the four different background models after one hour.

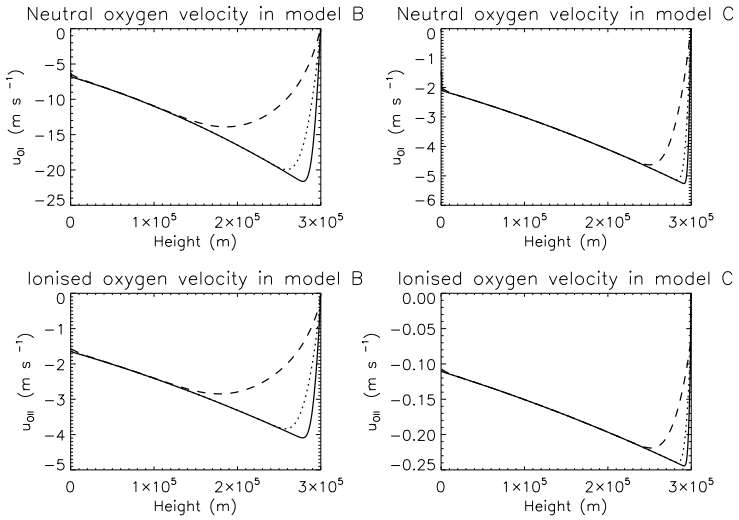

Figure 4.11: The neutral and ionised oxygen velocities in the background models B and C. The solid curve is reached after one minute, the dotted curve is reached after five minutes and the dashed curve is reached after one hour.

charge exchange) as follows,

$$\text{Collision term} = \nu_{ji}(u_j - u_i) \tag{4.9}$$

$$\text{Charge exchange (neutral oxygen)} = \frac{n_2}{n_1}\, u_2\, n_H C_{REC} - u_1\, n_p C_{ION} \tag{4.10}$$

$$\text{Charge exchange (ionised oxygen)} = \frac{n_1}{n_2}\, u_1\, n_p C_{ION} - u_2\, n_H C_{REC} \tag{4.11}$$

in units m s^{-2}.

Figure 4.12 shows that hydrostatic equilibrium is far from being reached. The neutral gas initially falls with its terminal velocity, i.e. the velocity of a gas that only feels gravity and friction. The ionised gas falls faster than its terminal velocity due to the large charge exchange term that pulls the gas towards the sun with a force almost four times the gravitational force. At the upper boundary, both the neutral and ionised velocities are fixed to zero. Since no material is permitted to enter the slab trough the upper boundary, a pressure gradient arises as the gas falls towards the sun, and the velocity of the gas diminish during the gravitational settling. The gas in this part of the slab therefore reaches hydrostatic equilibrium before it is reached by the rest of the slab. This situation then propagates to the lower parts of the atmosphere until a steady state is reached much later, and the system remain close to hydrostatic equilibrium through the whole atmosphere layer.

The reason why the ionised oxygen velocity is smaller than the neutral oxygen velocity in model B has its origin in the collision frequencies (see section 2.5). The force balance for neutral and ionised oxygen in figure 4.12 shows that friction due to collisions with the background is one of the main forces during the gravitational settling, together with gravity and charge exchange with the background. Because the collision frequency for proton-ion collisions is much stronger than the rate for neutral-neutral collisions, the ionised gas feels a stronger collisional friction than the neutral, and in spite of the large negative contribution from the charge exchange term, it falls slower than the neutral.

Also in model C the ionised gas falls slower than the neutral, and again, this is due to the difference between the proton-ion and the neutral-neutral collision frequencies. In fact, as shown in the force balance plot in figure 4.13 the contribution from collisions is important for both neutral and ionised oxygen. The contribution from charge exchange is also important for the force balance, and hence the terminal velocities are determined by both collisions and charge exchange. In model C, compared to model B, there are more protons and more ionised oxygen particles. We have therefore even

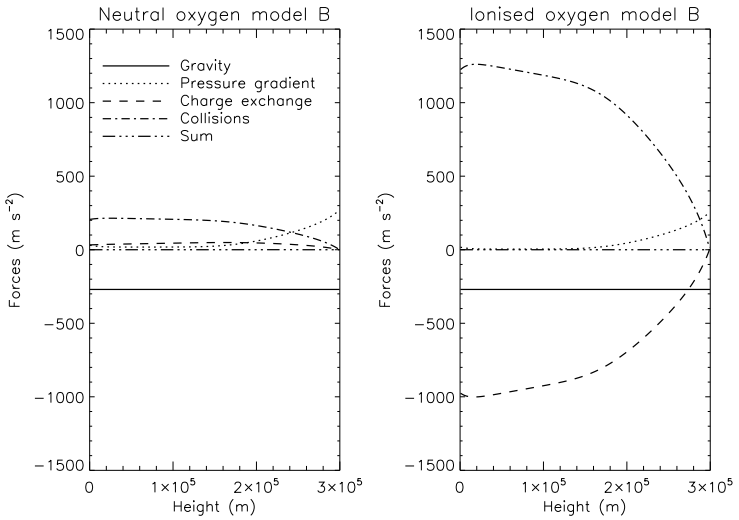

Figure 4.12: The force balance for neutral and ionised oxygen after one hour in model B. (The contribution from the electric field is approximately zero.)

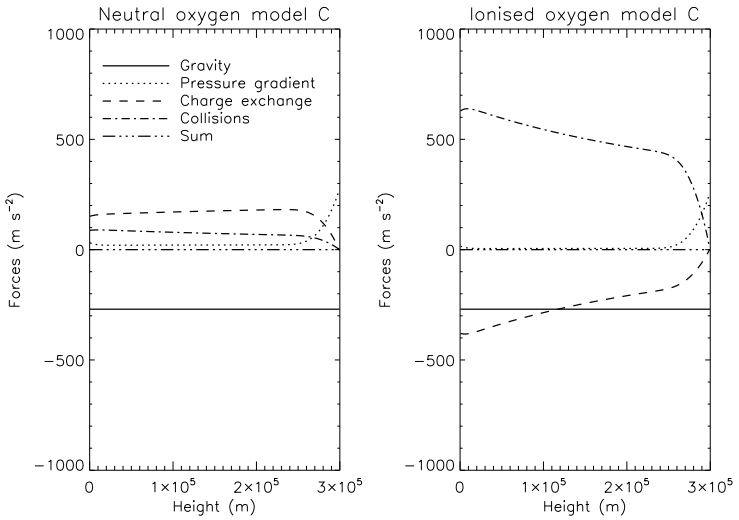

Figure 4.13: The force balance for neutral and ionised oxygen after one hour in model C. (The contribution from the electric field is approximately zero.)

	Model A	Model B	Model C	Model D
P_{12} (s^{-1})	8.7(-5) - 5.7(-3)	8.0(-4) - 4.6(-2)	9.5(-3) - 4.8(-1)	4.1(-2) - 1.9(0)
P_{21} (s^{-1})	6.4(-4) - 5.2(-4)	5.9(-3) - 4.2(-3)	7.0(-2) - 4.4(-2)	3.1(-1) - 1.7(-1)

Table 4.2: Ionisation (P_{12}) and recombination (P_{21}) rates for silicon. The first values are lower boundary rates while the second ones are upper boundary rates. $8.7(-5)$ means 8.7×10^{-5}.

more proton-ion collisions which leads to smaller velocities for the ions and, due to the charge exchange process, smaller velocities also for the neutrals.

For ionised oxygen the contribution from charge exchange with the background diminishes from model B to model C, while for neutral oxygen the contribution from charge exchange increases from model B to C. The amount of ionised oxygen in model B is small compared to the amount of neutral oxygen and hence the effect that one ionising neutral oxygen atom has on the whole group of ionised oxygen is much larger than the effect that a recombining ionised oxygen has on the group of neutrals. When neutral and ionised oxygen are more equally abundant, as in model C where the ionisation degree is approximately 50%, the absolute value of the charge exchange terms in the force balance (figure 4.13) is similar for neutral and ionised oxygen. Since neutral oxygen has higher negative velocities than ionised oxygen, the contribution from charge exchange is negative for ionised oxygen and positive for neutral oxygen. With an increasing ionisation degree of the background, the positive contribution to the force balance from charge exchange for neutral oxygen is also increasing. On the other hand, the negative contribution from charge exchange to the ionised oxygen force balance decreases (in absolute value).

4.2.2 Silicon

Model A When the gravitational settling of silicon is studied in model A, one sees that it takes more than 24 hours before the ionisation degree of the steady state solution is reached, but the ionisation degree is close to the steady state ionisation degree after one hour. Figure 4.14 shows the ionisation degree after one minute, five minutes, one hour and after steady state is reached. The ionisation degree increases during the first hour, but then it decreases slowly until it reaches the steady state value. The silicon ionisation and recombination rates in model A-D are given in table 4.2.

The absolute and relative silicon abundances are shown in figure 4.15. The relative silicon abundance increases, at least in some parts of the atmosphere

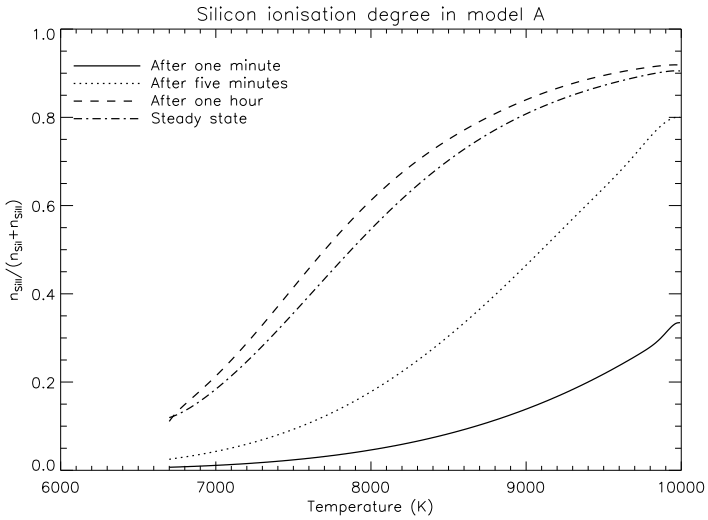

Figure 4.14: The silicon ionisation degree in model A after one (solid curve), five (dotted curve) and sixty minutes (dashed curve), and after steady state is reached (dash dotted curve).

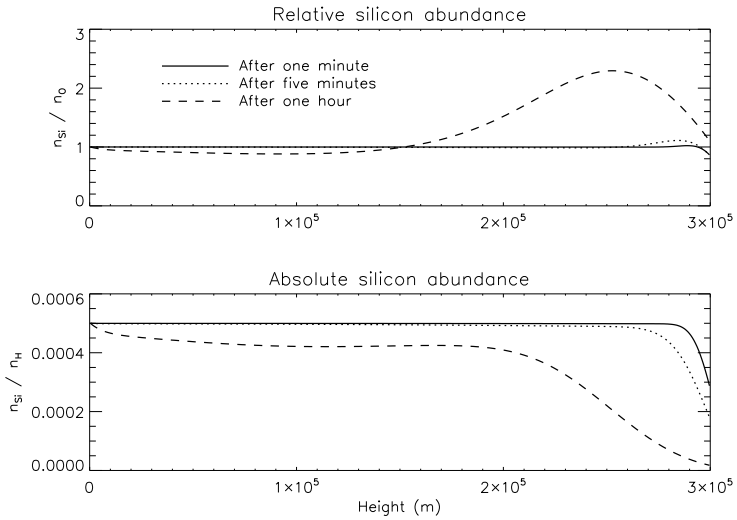

Figure 4.15: The absolute and relative silicon abundances in model A after one (solid curve), five (dotted curve) and sixty minutes (dashed curve).

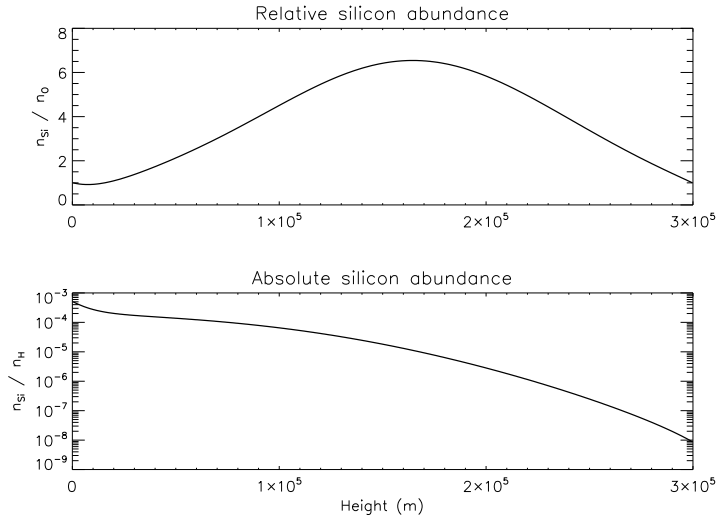

Figure 4.16: Maximum relative silicon abundance in model A, reached at 2×10^4s, with the corresponding absolute abundance.

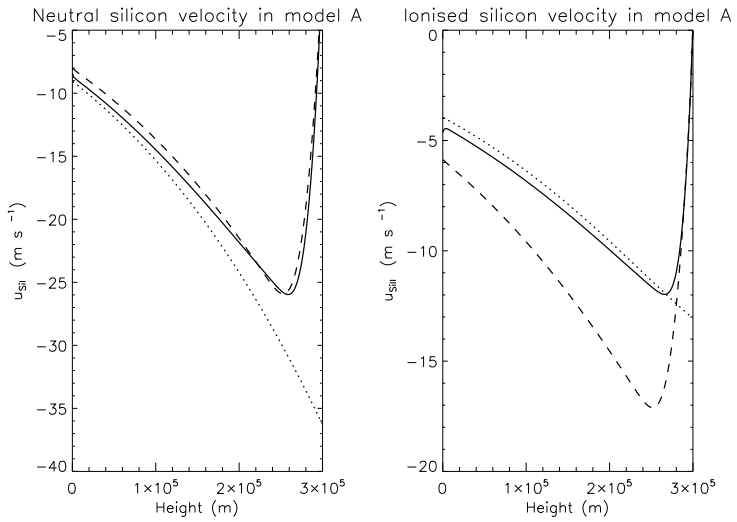

Figure 4.17: Silicon velocities (solid curve), terminal silicon velocities given by equation 4.15 (dotted curve) and oxygen velocities (dashed curve) after five minutes in model A.

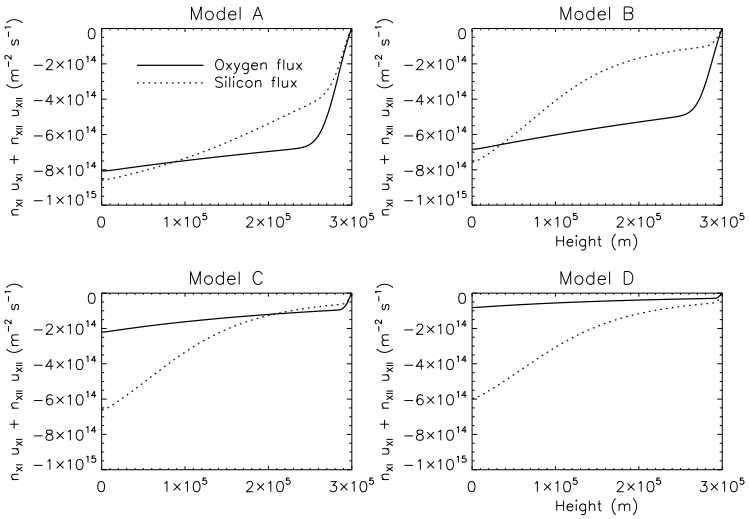

Figure 4.18: The oxygen (solid curve) and silicon (dotted curve) fluxes after five minutes in all four background models.

layer, during the gravitational settling. The maximum value of the relative silicon abundance after one hour is 2.3. Figure 4.15 also shows how the absolute abundance of silicon decreases during the first hour of gravitational settling, and it is clear that there is still a sizable amount of silicon left after one hour, also in the upper part of the atmosphere layer where the relative silicon abundance is highest. The abundance continues to increase until it reaches a maximum value of 6.5 after approximately 2×10^4s, as shown in figure 4.16, and then it decreases until it reaches the steady state value at 2×10^5s. However, when the relative abundance is maximum, the silicon density is strongly reduced due to the gravitational settling, and where the relative abundance is highest, the absolute abundance is reduced by a factor of fifty. The maximum relative abundance of more than 6, therefore represents a gas strongly depleted in both silicon and oxygen.

The neutral and ionised silicon velocities are shown together with their terminal velocities in figure 4.17. The terminal velocities will be discussed later in this section. The neutral silicon velocity is larger, in absolute value, than the ionised silicon velocity, but they are of the same order of magnitude. Figure 4.18 shows that the silicon flux (in absolute value) is smaller than the oxygen flux in the upper part of the atmosphere after five minutes in model A.

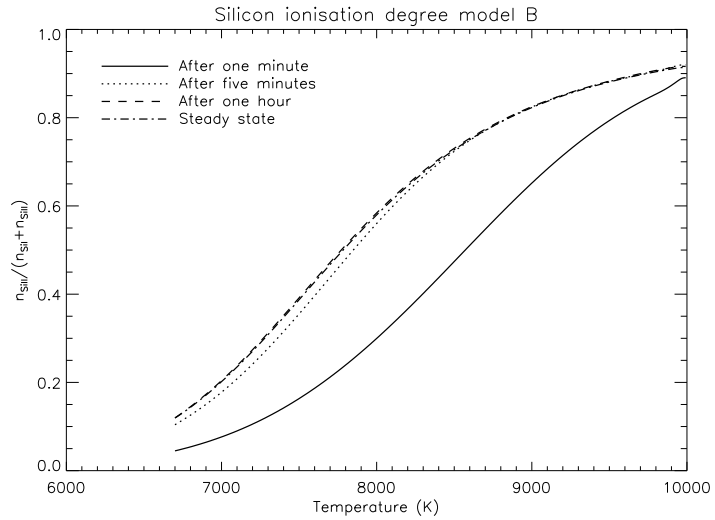

Figure 4.19: The silicon ionisation degree in model B after one (solid curve), five (dotted curve) and sixty minutes (dashed curve), and after steady state is reached (dash dotted curve). The ionisation degree after sixty minutes and the steady state ionisation degree overlap.

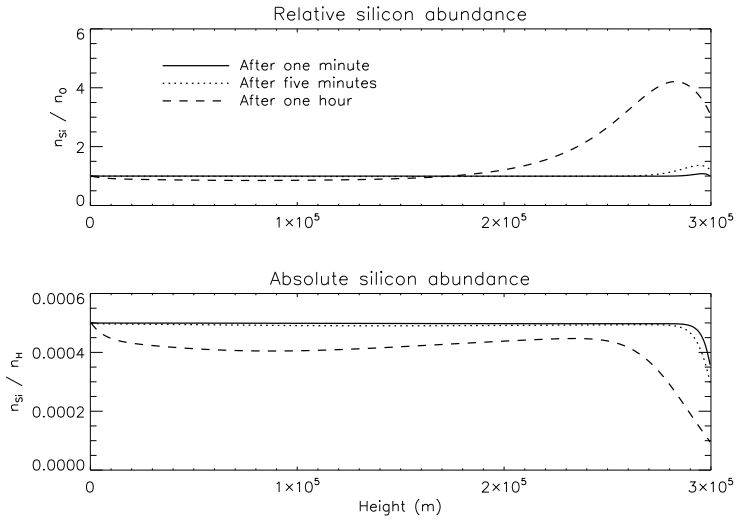

Figure 4.20: The absolute and relative silicon abundances in model B after one (solid curve), five (dotted curve) and sixty minutes (dashed curve).

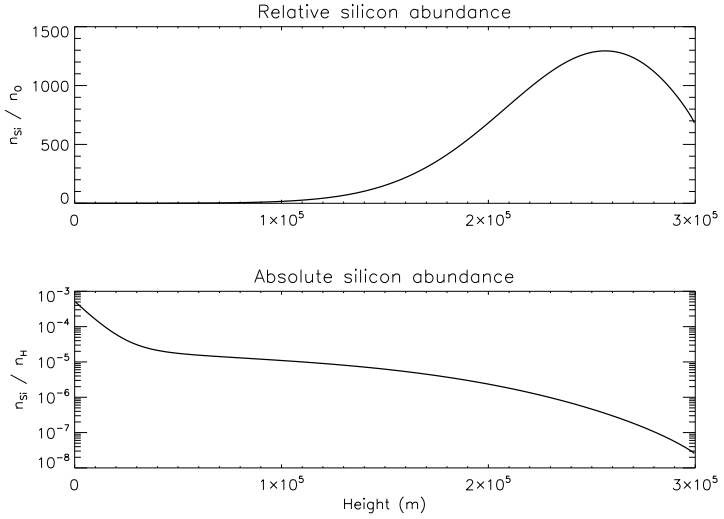

Figure 4.21: Maximum relative silicon abundance in model B, reached at 5×10^4s, with the corresponding absolute abundance.

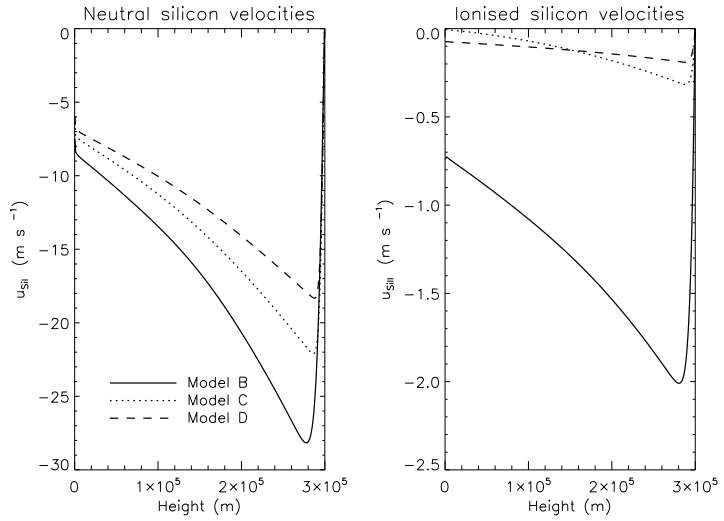

Figure 4.22: The silicon velocities after five minutes in model B (solid curve), C (dotted curve) and D (dashed curve).

Model B In model B, the ionisation process is much faster than in model A. The ionisation degree after one, five and sixty minutes are shown together with the steady state ionisation degree in figure 4.19, and we see that silicon is very close to its steady state ionisation degree already after five minutes.

The abundance enhancement is much larger in this model compared to model A. The relative silicon abundance in figure 4.20 shows that the maximum value of the relative silicon abundance is more than 4 after one hour. The absolute silicon abundance in the same figure shows that the silicon density, where this maximum value is reached, is only reduced by approximately 50%. The relative silicon abundance continues to increase the first 5×10^4s. At this time it reaches the maximum value of 1.3×10^3 shown in figure 4.21, before it starts to decrease towards the steady state value. The absolute silicon abundance is reduced by a factor of thousand at this late time.

As shown in figure 4.22, both the neutral and ionised silicon velocities are reduced in absolute value compared to model A, but the reduction of the neutral silicon velocity is smaller than the one in the ionised silicon velocity, and the former is now one order of magnitude larger than the latter. Also the neutral silicon flux is larger (in magnitude) than the ionised silicon flux, even if there are more ionised than neutral silicon in most of the atmosphere layer.

The absolute value of the oxygen flux is only reduced by approximately 20% from model A, but the absolute value of the silicon flux is strongly reduced, particularly in the upper part of the atmosphere (see figure 4.18). The difference between the silicon and the oxygen fluxes is therefore much larger in this model compared to model A.

Model C In model C the steady state ionisation degree is reached during the first minute of the gravitational settling. The silicon ionisation degree is shown in figure 4.23, where we see that it is slightly different from the steady state ionisation degree in model A.

As one can see from figure 4.24, we also get enrichment of silicon in model C. After one hour, though, the abundance enhancement is much smaller than in model B, and the maximum value of the relative silicon abundance, as shown in figure 4.25, is also lower in this model than in model B. The relative abundance after one hour is at most between 1.1 and 1.2, and the maximum relative abundance, after 2×10^4s, is between 1.2 and 1.3.

The absolute values of the silicon velocities continue to decrease with increasing ionisation degree of the background, and the velocity difference between neutral and ionised silicon continues to increase. Neutral silicon flows approximately hundred times faster than ionised silicon towards the

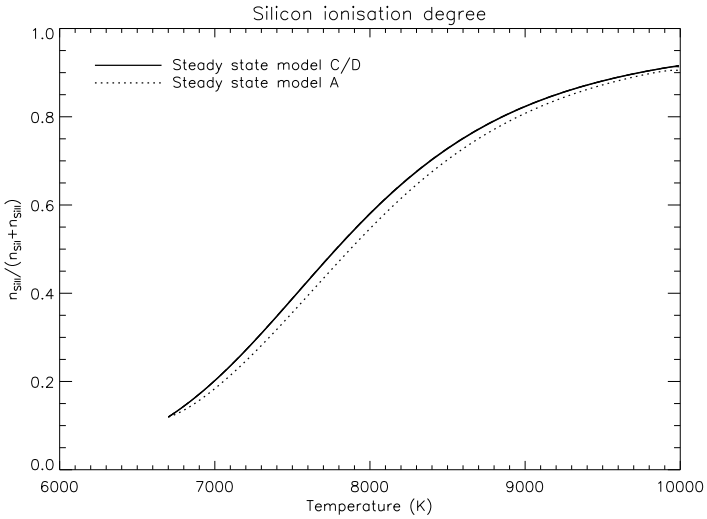

Figure 4.23: The steady state ionisation degree for silicon in model C and D (solid curve) compared to model A (dotted curve).

sun (see figure 4.22).

As a consequence of the velocity reduction, the absolute value of the silicon flux is also reduced from model B to model C, but not as much as the reduction of the absolute value of the oxygen flux (see figure 4.18). The difference between the two fluxes in the upper part of the atmosphere, where the silicon flux is smaller than the oxygen flux, is reduced compared to model B, and the difference in the lower part, where the oxygen flux is smaller (in magnitude) than the silicon flux, is increased.

Model D As in model C, also in model D the steady state ionisation degree is reached during the first minute of the gravitational settling, and as shown in figure 4.23, the steady state ionisation degree in model D is equal to the ionisation degree in model C. The relative silicon abundance in figure 4.26 shows that we do not obtain any enrichment of silicon in this model.

Both the neutral and ionised silicon velocities are further reduced, in absolute value, from model C to model D, but the difference between them is still two orders of magnitude. The oxygen flux is in this model smaller, in magnitude, than the silicon flux over the whole atmosphere layer. Figure 4.18 shows that the absolute value of the oxygen flux is reduced by more than 50% from model C to model D, while the silicon flux has hardly felt any reduction at all.

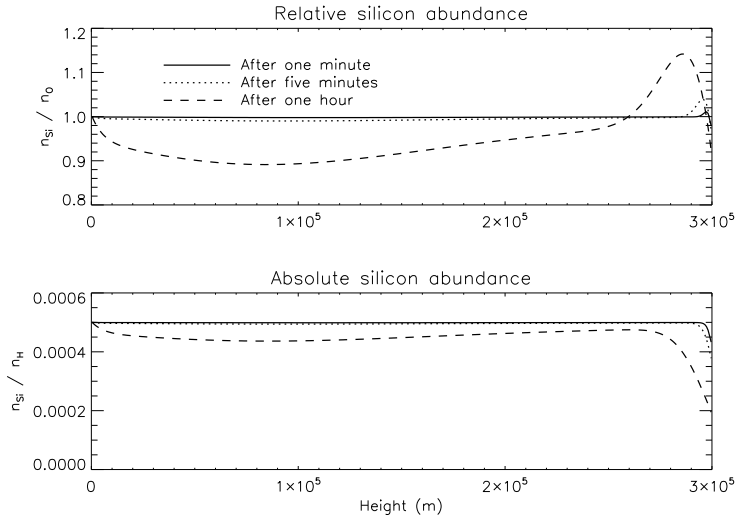

Figure 4.24: The absolute and relative silicon abundances in model C after one (solid curve), five (dotted curve) and sixty minutes (dashed curve).

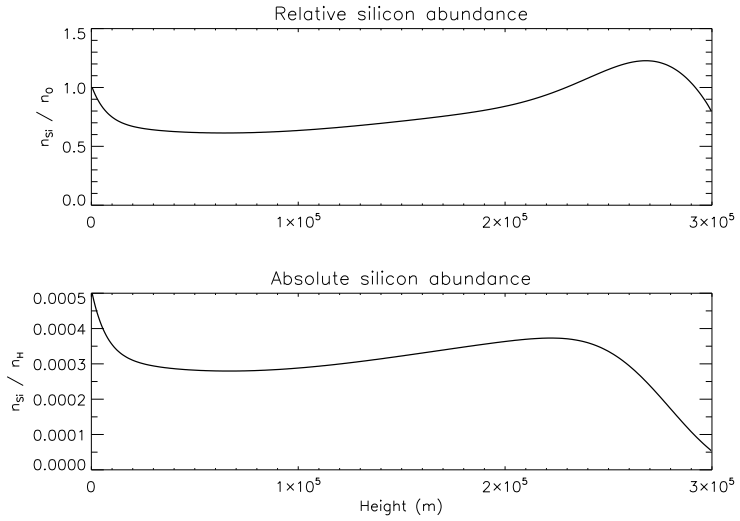

Figure 4.25: Maximum relative silicon abundance in model C, reached at 2×10^4s, with the corresponding absolute abundance.

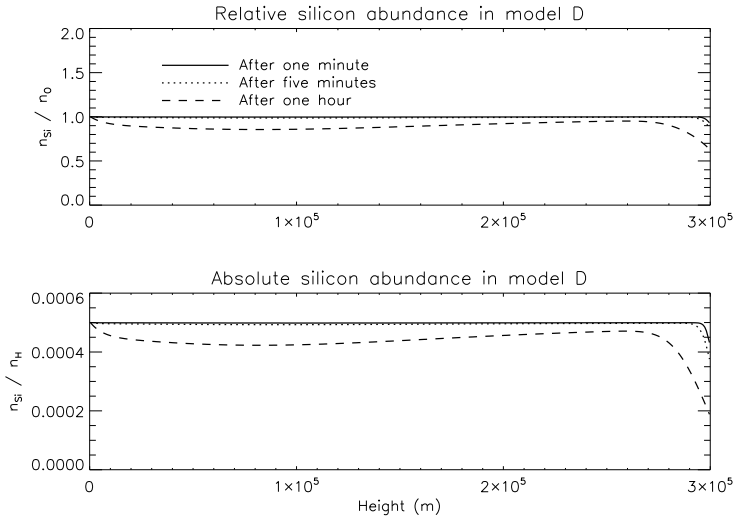

Figure 4.26: The absolute and relative silicon abundances in model D after one (solid curve), five (dotted curve) and sixty minutes (dashed curve).

Discussion The reason why the ionisation process is so slow in model A is due to the very low electron density, which again is caused by the low ionisation degree of the background (low proton density) in this model. In fact, as given by equation 2.27 and 2.32, the ionisation and recombination rates depend on the electron (proton) density. Since it is not only the ionisation rate, but also the recombination rate that depends on the proton density, the major effect of an increase of the hydrogen ionisation degree from model A to D is not a difference between the silicon ionisation degrees, but rather a longer ionisation time for less ionised backgrounds.

There is though, as shown in figure 4.23, a small difference between the steady state ionisation degree in model A and the ionisation degrees in the other three models. The steady state ionisation degrees in model B, C and D are all equal the ionisation degree at ionisation equilibrium, while the steady state ionisation degree in model A is not. Ionisation equilibrium occurs when both the left hand side terms of the continuity equation (2.1) are negligible, and the ionisation and recombination terms cancel,

$$0 = n_j \; P_{ji} - n_i \; P_{ij} \; . \tag{4.12}$$

The ionisation degree at ionisation equilibrium is thus given by

$$\frac{n_2}{n_1 + n_2} = \frac{P_{12}}{P_{12} + P_{21}} \; . \tag{4.13}$$

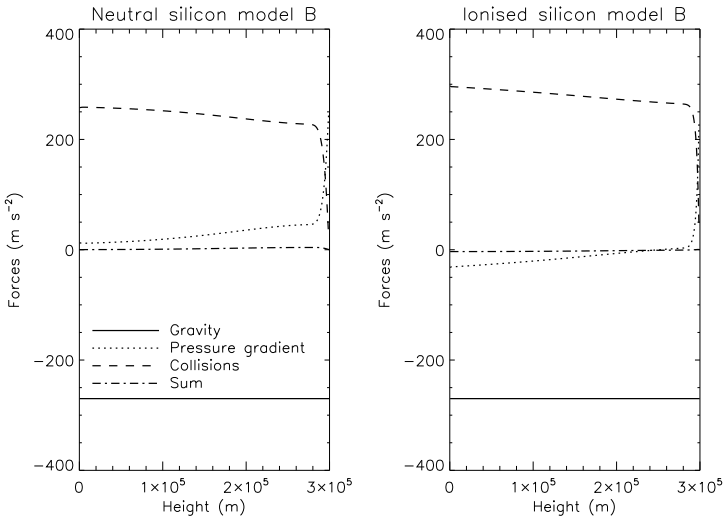

Figure 4.27: The force balance for neutral and ionised silicon after five minutes in model B. (The contribution from the electric field is approximately zero.)

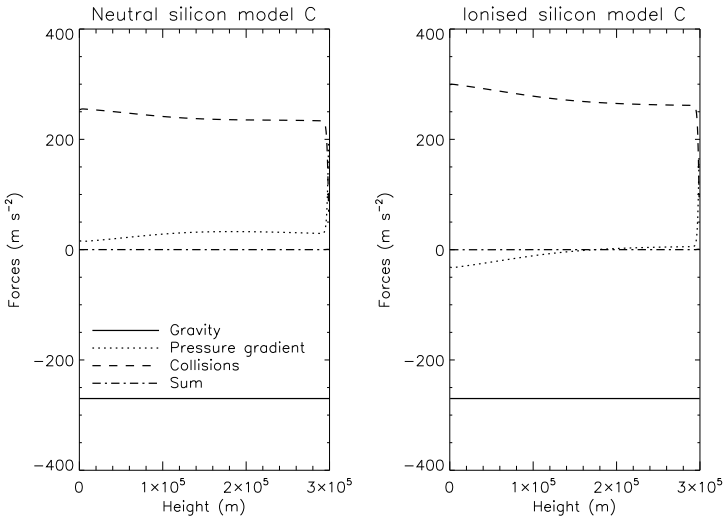

Figure 4.28: The force balance for neutral and ionised silicon after five minutes in model C. (The contribution from the electric field is approximately zero.)

In fact, the advection term is at least two orders of magnitude smaller than the ionisation and recombination terms in model B, C and D, while in model A, due to the low electron density, the ionisation and recombination terms are of the same order of magnitude as the advection term.

The ionisation degree of the backgrounds do not vary with time during the gravitational settling of the minor constituents. Since the ionisation time of silicon is similar to the settling time of silicon in model A, both of magnitude 10^3s, it could be more consistent if the ionisation process in the background also took place during the gravitational settling of silicon in this model. The silicon ionisation rate depends on the electron (proton) density, and since the ionisation rate for hydrogen in model A is low (see table 4.1), the hydrogen ionisation process is slow and the silicon ionisation process would be even slower. If the ionisation rate for silicon decreases, the settling time decreases (neutral particles flow faster than ionised particles), and we expect the relative silicon abundance to be smaller than what we get with fixed hydrogen ionisation degree. Due to the computational complications, in this work we do not study gravitational settling of minor constituents in backgrounds where the ionisation degree changes with time. We could have studied the gravitational settling of silicon, starting with (or close to) ionisation equilibrium. However, by starting with ionisation equilibrium for silicon, we expect the absolute value of the silicon flux, during the first hour of the gravitational settling, to be smaller than what we obtain with an ionisation degree that increases with time. Hence, we would also expect the abundance enhancement to be larger.

The silicon force balance is very similar in all four background models. The force balances after five minutes in model B and C are shown in figure 4.27 and 4.28, respectively. We see that it is almost only the collisional friction that balances the gravitational force for both neutral and ionised silicon. This means that both neutral and ionised silicon velocities in figure 4.17 and 4.22 are close to their terminal velocities. When only gravity and collisional friction balance each other, the momentum equation (2.2) simplifies to

$$0 = g + \nu_{iH}(u_H - v_i) + \nu_{ip}(u_p - v_i) \ , \tag{4.14}$$

where $i = 1, 2$ represents the neutral and ionised gas, respectively. The neutral and ionised terminal velocities v_1 and v_2 can therefore be written

$$v_i = \frac{g + \nu_{iH}u_H + \nu_{ip}u_p}{\nu_{iH} + \nu_{ip}} \approx \frac{g}{\nu_{iH} + \nu_{ip}} \ . \tag{4.15}$$

For neutral silicon we have that ν_{1p} is slightly stronger than ν_{1H}, and that $\nu_{1H} \propto n_H$ and $\nu_{1p} \propto n_p$. Hence, equation 4.15 explains why the neutral

silicon velocity decreases in absolute value with increasing ionisation degree of the background from model A to D. Concerning ionised silicon, the collision frequency ν_{2p} is not directly proportional to the proton density n_p, and hence it is not so easy to predict what happens with the ionised silicon velocity when the ionisation degree of the background changes.

The largest change in the silicon fluxes is from model A to model B, where the shape of the flux profile also is altered. This is because the fluxes in figure 4.18 are plotted after five minutes, and the silicon ionisation degree in model A is much lower than the ionisation degrees in the other models after five minutes. Neutral silicon flows faster than ionised silicon, and since there are much more neutral silicon in model A than in model B, C and D after five minutes, the absolute value of the total flux is larger in this model compared to the other three at this time.

The silicon abundance enhancement is largest in model B, and we need to explain why it does not increase from model B to C. To do this we have to remember that the gas flows with its terminal velocity, and that the collisional friction with the background therefore determines the flow speed. The proton-ion collision frequency depends on the proton density n_p, which increases significantly from model B to C. The ionised silicon velocity therefore diminishes from model B to C. The neutral silicon velocity also diminishes from model B to C, since the collisions between neutral silicon and protons are slightly stronger than the collisions between neutral silicon and neutral hydrogen. Hence, one expects the abundance enhancement to increase. The reason why it does not increase from model B to C is because the ionisation degree of an element constitutes the main contributor to the flow speed. That is, since the difference between the neutral and ionised gas velocities is so large, an increase in the ionisation degree causes a strong decrease in the flow speed. Due to the charge exchange interaction between oxygen and hydrogen the oxygen ionisation degree is increased by a factor of seven from model B to C, while the silicon ionisation degree remains constant. Hence, the decrease in the absolute value of the oxygen is so large that the abundance enhancement diminishes even if the absolute value of the silicon flux also decreases from model B to C.

4.2.3 Magnesium

Magnesium has similar weight and similar first ionisation potential (see table 2.1) as silicon. When we study the gravitational settling of magnesium, we therefore obtain almost the same results as for silicon. Magnesium is enriched in model A, B and C, but strongest in model B. Model D does not produce any abundance enhancement for magnesium. The values of the

Time (s)	Model A	Model B	Model C	Model D
60	1.1	1.1	1.01	0.97
3.0×10^2	1.2	1.4	1.03	0.93
3.6×10^3	2.9	4.2	1.12	0.79
t_{max} [1]	28	2.2×10^3	1.23	-

Table 4.3: The relative magnesium abundance after one, five and sixty minutes, together with the maximum abundance enhancement in each model. Since we do not obtain any abundance enhancement in model D, the relative abundances for this model are taken at the upper boundary.

Time (s)	Model A	Model B	Model C	Model D
60	0.91	0.92	0.98	0.93
3.0×10^2	0.78	0.84	0.94	0.86
3.6×10^3	0.38	0.48	0.78	0.60
t_{max} [1]	0.0032	0.00064	0.38	-

Table 4.4: The absolute magnesium abundances that correspond to the maximum relative abundances after one minute, five minutes, one hour and at $t = t_{max}$, all divided by the absolute abundance at the lower boundary (5×10^{-4}).

relative magnesium abundances after one, five and sixty minutes are listed in table 4.3 together with the the maximum abundance enhancement for each model. The correspondent absolute abundances are listed in table 4.4.

The velocities and the force balance are also basically the same as for silicon. The neutral and ionised magnesium velocities are both close to the terminal velocities. The former is higher than the latter, and both are gradually reduced from model A to D.

4.2.4 Iron

The first ionisation potential of iron is similar to that of silicon (see table 2.1), but iron is twice as heavy as silicon, and the silicon collision frequencies are therefore twice the iron collision frequencies (see section 2.5). Hence, because we expect collisional friction to be the main force to balance gravity, we expect the iron velocities to be approximately twice the silicon velocities.

[1] The maximum abundance enhancement is reached at different times for each model. In model A $t_{max} = 3 \times 10^4$ s, in model B $t_{max} = 8 \times 10^4$ s and in model C $t_{max} = 2 \times 10^4$ s.

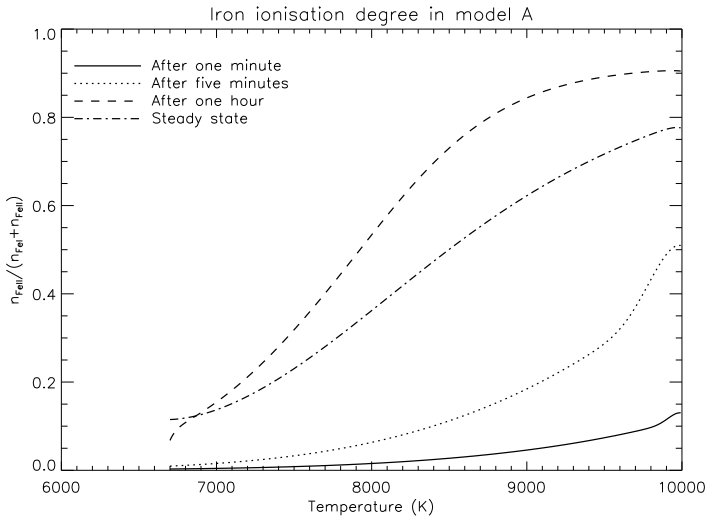

Figure 4.29: The ionisation degree of iron after one minute (solid curve), five minutes (dotted curve), one hour (dashed curve) and after steady state is reached (dash dotted curve) in model A.

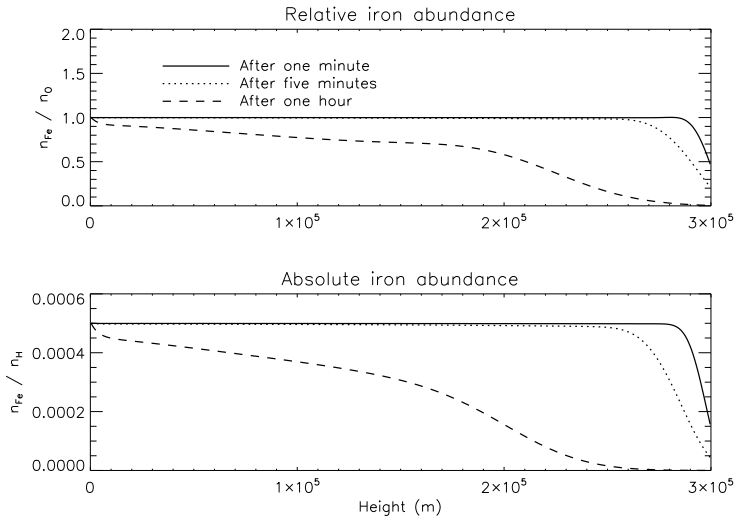

Figure 4.30: The absolute and relative iron abundance in model A after one (solid curve), five (dotted curve) and sixty minutes (dashed curve).

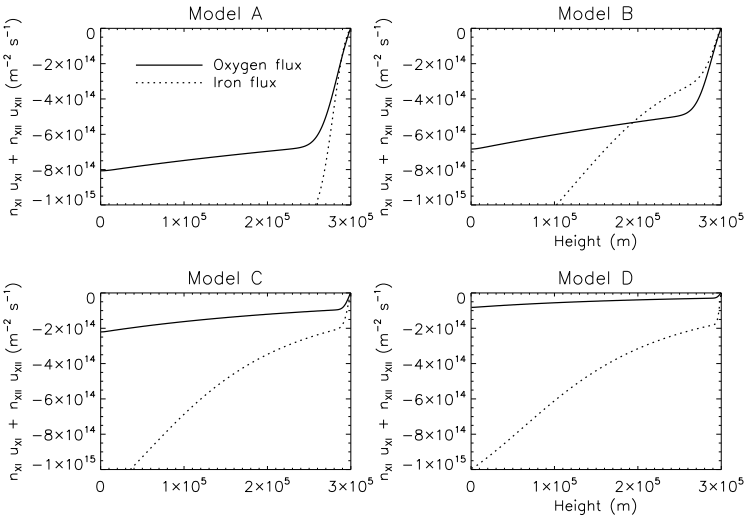

Figure 4.31: Oxygen (solid curve) and iron (dotted curve) fluxes in all four background models after five minutes.

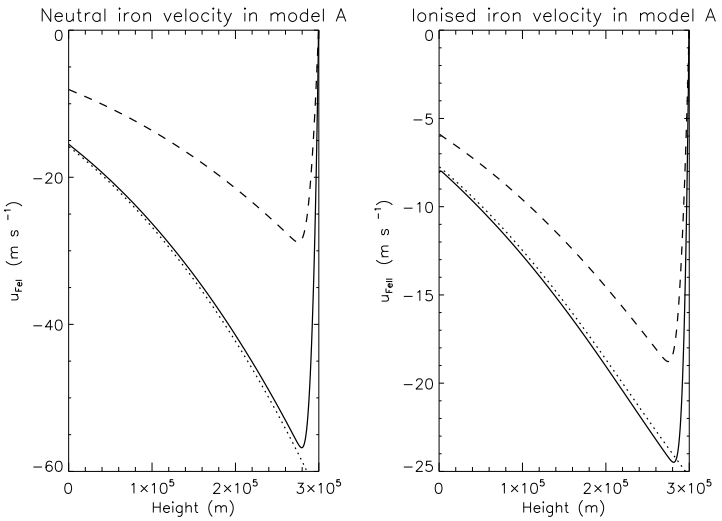

Figure 4.32: Iron velocities (solid curve), terminal iron velocities given by equation 4.15 (dotted curve) and oxygen velocities (dashed curve) after one minute in model A.

	ν_{1H}/n_H	ν_{1p}/n_p	ν_{2H}/n_H	ν_{2p}/n_p
Silicon	1.65(-16)	2.11(-16)	7.42(-17)	4.91(-14)
Iron	9.46(-17)	1.33(-16)	3.77(-17)	2.49(-14)

Table 4.5: Neutral-neutral, neutral-ion and proton-ion collision frequencies for silicon and iron in units of $m^3\ s^{-1}$. Index 1 represents neutral iron (silicon) and index 2 ionised iron (silicon). $1.65(-16)$ means 1.65×10^{-16}.

The collision frequencies for iron and silicon, divided by the proton or neutral hydrogen density are given in table 4.5.

As for silicon the ionisation process of iron is slow in model A. This is illustrated in figure 4.29 where the ionisation degree after one, five and sixty minutes are shown together with the steady state ionisation degree. The absolute and relative iron abundances in figure 4.30 show that we do not get any abundance enhancement of iron in model A. In fact the absolute value of the iron flux after five minutes is larger than the absolute value of the oxygen flux over the whole atmosphere layer, as shown in figure 4.31. After one hour, this is not true anymore, the iron flux (in absolute value) gets smaller than the oxygen flux in some parts of the atmosphere layer. At this time though, the iron flux has been very high for one hour, and the small difference between the iron and oxygen flux after one hour is not enough to enrich iron compared to oxygen. The neutral and ionised iron velocities after one minute in model A are compared with their corresponding terminal velocities and the oxygen velocities in figure 4.32. Both neutral and ionised iron velocities are larger than the oxygen velocities. They are also larger than the silicon velocities, but not by more than a factor of two.

The ionisation process is also slow in model B. Figure 4.33 shows that iron needs approximately one hour to reach its steady state ionisation degree. The collisional friction in this model is large enough to create an abundance enhancement of iron. From figure 4.34 we see that the relative iron abundance increases only very little during the first five minutes, but that it is enhanced to 1.4 after one hour. This value is the maximum abundance enhancement we obtain for iron, and it is very small compared to the maximum value of the relative silicon abundance in the same model of more than thousand. However, the absolute iron abundance is not even reduced by a factor of two, while the absolute silicon abundance is reduced by a factor of thousand when the maximum relative abundance is reached. The iron velocities after one minute in model B, C and D are shown in figure 4.35. They are all approximately twice the corresponding silicon velocities (see figure 4.22). From the upper right panel in figure 4.31 we see that the iron flux is smaller

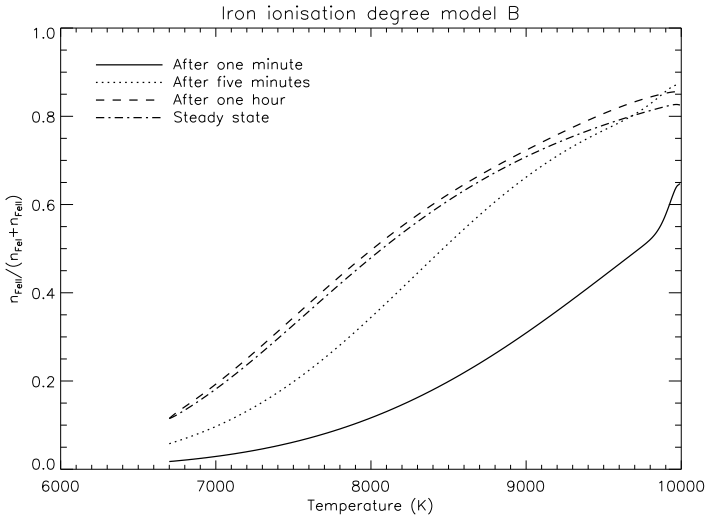

Figure 4.33: The ionisation degree of iron after one minute (solid curve), five minutes (dotted curve), one hour (dashed curve) and after steady state is reached (dash dotted curve) in model B.

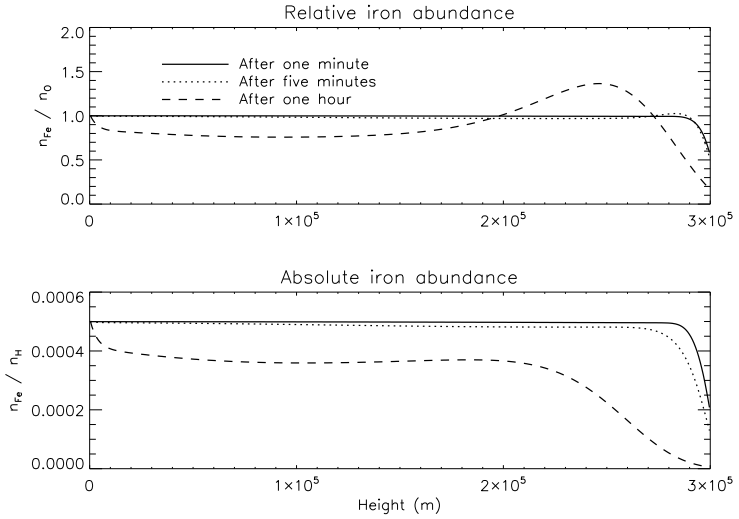

Figure 4.34: The absolute and relative iron abundances in model B. The value after one hour corresponds to the maximum abundance enhancement of iron.

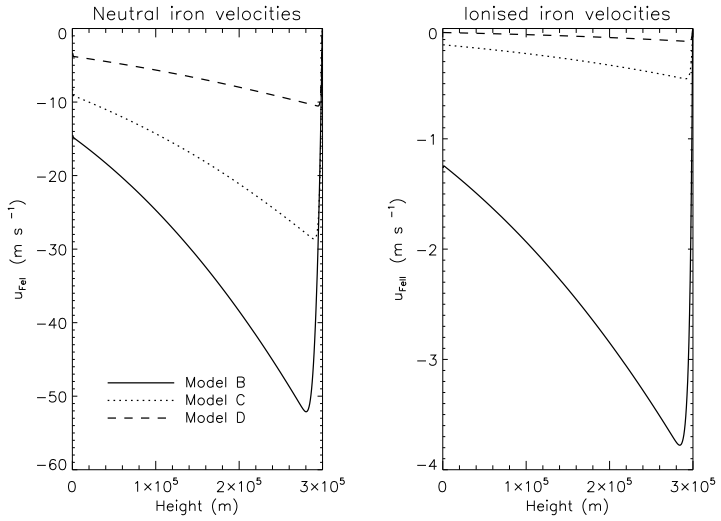

Figure 4.35: The neutral and ionised iron velocities after one minute in model B, C and D.

in magnitude than the oxygen flux after five minutes.

In model C and D the steady state ionisation degree is reached during the first five minutes. As for silicon, these two ionisation degrees are equal, but they are different from the steady state ionisation degree in model A. This is shown in figure 4.36. The absolute value of the oxygen flux is smaller than the absolute value of the iron flux through the whole atmosphere layer. In fact, we do not obtain any abundance enhancement of iron in model C, as shown in figure 4.37. This is true also for model D, where the difference between the oxygen and iron fluxes is even larger than in model C (see figure 4.31).

All the results we obtain for iron are similar to the silicon results except for the relative abundances. The ionisation process is slow in model A and B due to the low electron density. The low electron density also causes the ionisation degree in model A to be different from the one at ionisation equilibrium. The force balance for both neutral and ionised iron is, as for silicon, dominated by gravity and collisions, and can be represented by the silicon force balance in figure 4.27. Both the neutral and ionised iron velocities should therefore be close to their terminal velocities given by equation 4.15, and the velocity plot in figure 4.32 ensures us that this is actually the case. Due to the difference between the silicon and iron collision frequencies, the silicon and iron velocities are different. The high iron velocities reduce the abundance enhancement of iron compared to silicon.

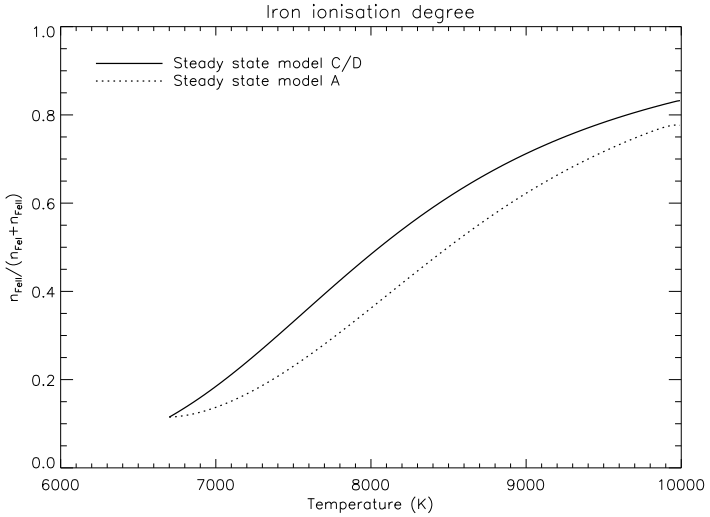

Figure 4.36: The steady state ionisation degree of iron in model C and D (solid curve) compared to model A (dotted curve).

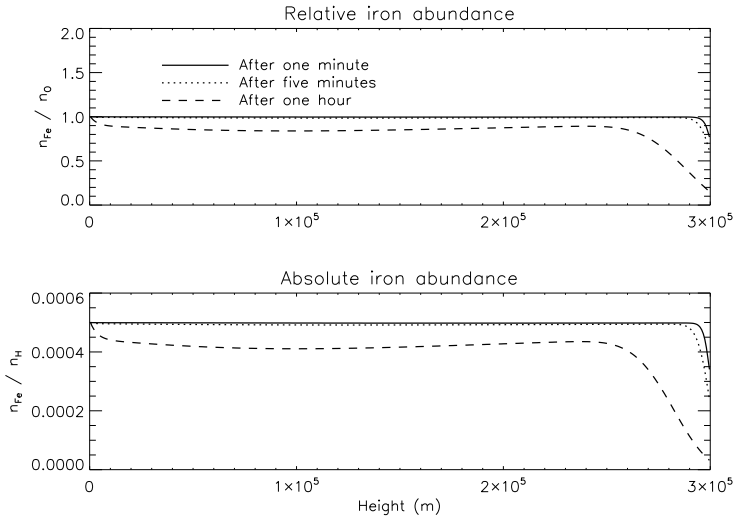

Figure 4.37: The absolute and relative iron abundances in model C.

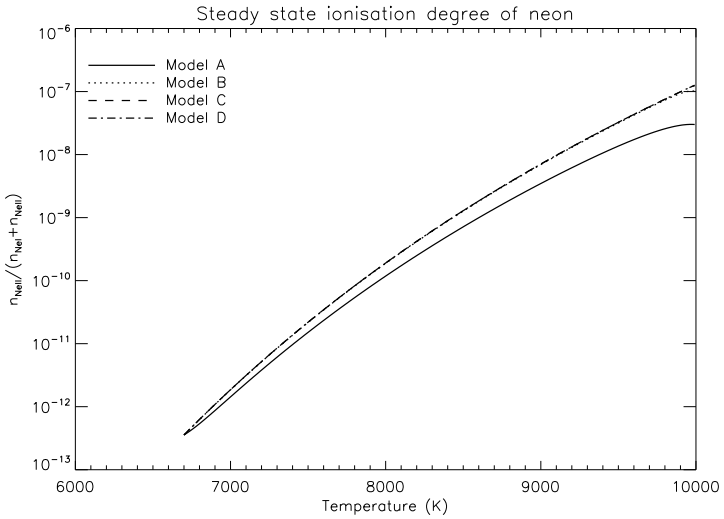

Figure 4.38: Steady state ionisation degrees of neon in all four background models. Only the one in model A is different from the other three.

4.2.5 Neon

The neon ionisation degree is extremely low in all four background models. Figure 4.38 shows that the steady state ionisation degrees in model B, C and D are 10^{-12} in the lower part and 10^{-7} in the upper part of the atmosphere layer. The steady state ionisation degree in model A is even lower, and this is the only model where the ionisation degree is different from the ionisation degree at ionisation equilibrium.

Figure 4.39 shows the absolute and relative neon abundances in model B after one, five and sixty minutes, and we see that the abundances decrease much more rapidly than any of the other minor constituents.

Figure 4.40 shows that the neon velocity is close to the terminal velocity, and that it has approximately the same value in model B as in model A. The ionised velocity is not of any importance, since neon is almost totally neutral. The total oxygen and neon fluxes in all four background models are shown in figure 4.41. The absolute value of the neon flux is much larger than the absolute value of the oxygen flux, and has almost the same value in all the four models.

The force balance for neutral neon is basically the same as for the other minor constituents. The main contributions are from gravity and collisional friction, and the velocity is therefore close to the terminal velocity, given by

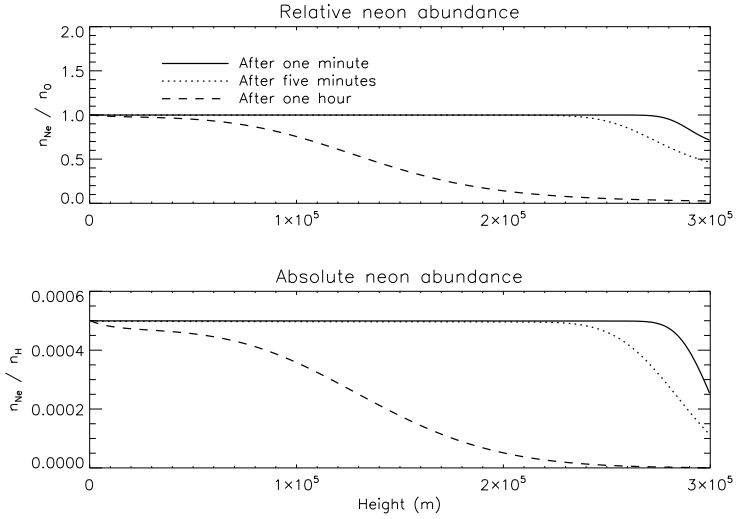

Figure 4.39: The absolute and relative neon abundances in model B.

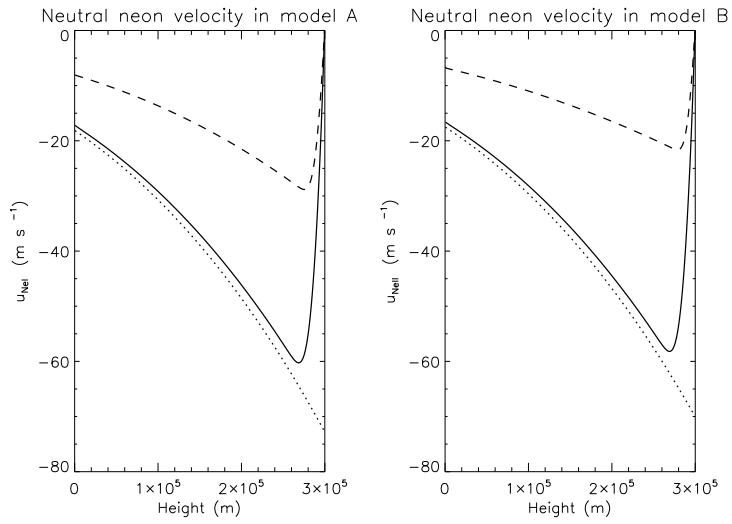

Figure 4.40: The neutral neon velocity (solid curve), terminal neon velocity given by equation 4.15 (dotted curve) and neutral oxygen velocity (dashed curve) after one minute in model A and B.

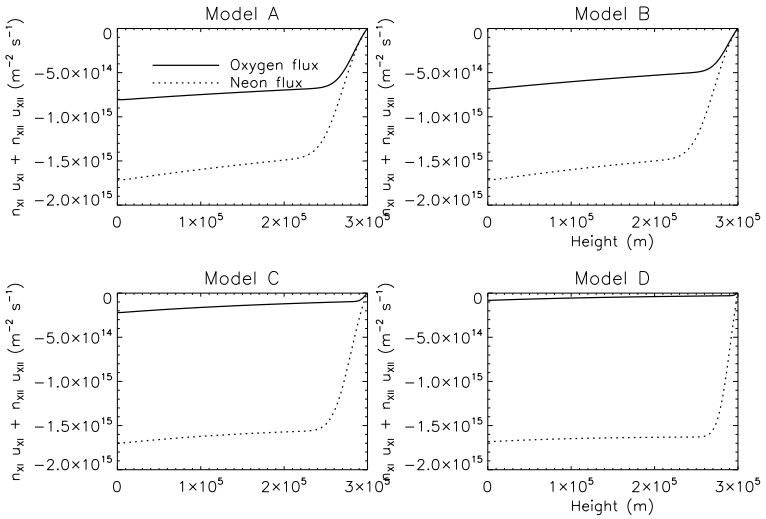

Figure 4.41: Oxygen (solid curve) and neon (dotted curve) fluxes in all four background models after five minutes.

equation 4.15.

The reason why the absolute value of the neon flux is so much larger than the absolute value of the total fluxes of the other minor constituents is because neon is almost totally neutral. Neutral-ion collisions are never strong enough to obtain a slower flux than the oxygen flux.

Chapter 5

Discussion

We have studied the gravitational settling of minor constituents in a chromosphere without any net outflow of hydrogen. At run start for the code the chromosphere is well mixed, with constant minor constituent abundances everywhere. Hence, in the upper part of the grid, the minor constituent abundances deviate strongly form their hydrostatic equilibrium abundances when starting the code. Due to gravity, the minor constituents fall towards the sun with negative velocities and only relative - not absolute - abundance enhancement is therefore possible. In fact, very small positive velocities are only reached by the neutral minor constituents when the whole system is in steady state, close to hydrostatic equilibrium, and the ionisation degree, as for hydrogen, causes counter flowing neutral and ionised gases.

The minor constituents are all highly depleted at steady state due to their small scale heights. Iron is depleted by a factor of 10^{28} while silicon is depleted by a factor of 10^{14}, compared to the photospheric abundances. We therefore assume that the system never reaches a steady state, and that some process in the solar atmosphere causes a regular mixing in order to achieve roughly the same chemical composition through the whole chromospheric layer. Furthermore, the measurements of the elemental abundances and the FIP fractionation effect come from observations of coronal and transition region lines (or from solar wind measurements), and not from the chromosphere where the abundances in this study are located. We therefore assume that the gas in the upper part of our grid is regularly transported up to the corona by some physical processes, for example by being rapidly and strongly heated. The time scale for these processes cannot be smaller than the one for the mixing process, because it would disturb the process of gravitational settling and thereby not allow for FIP fractionation.

If the absolute abundance of coronal iron measured by White et al. (2000) is representative for the absolute abundances of coronal low FIP elements in

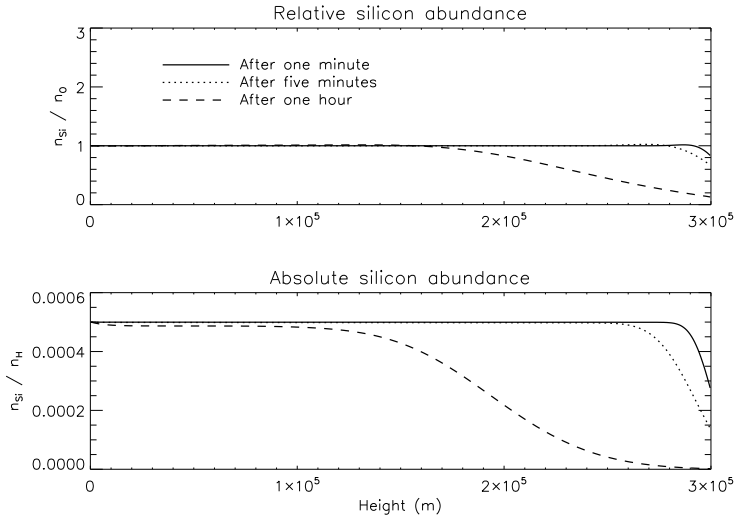

Figure 5.1: The absolute and relative silicon abundances in model E (totally neutral background).

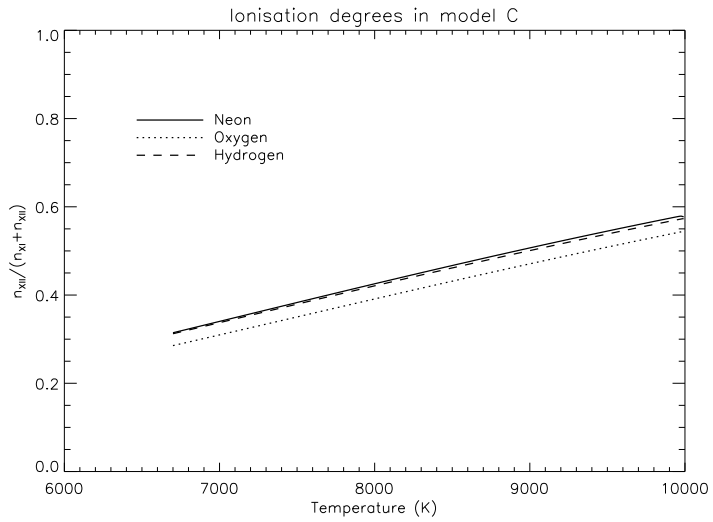

Figure 5.2: The neon (solid curve), oxygen (dotted curve) and hydrogen (dashed curve) ionisation degrees in model C, with the radiative ionisation rate of von Steiger and Geiss (1989) in addition to the collisional ionisation rate.

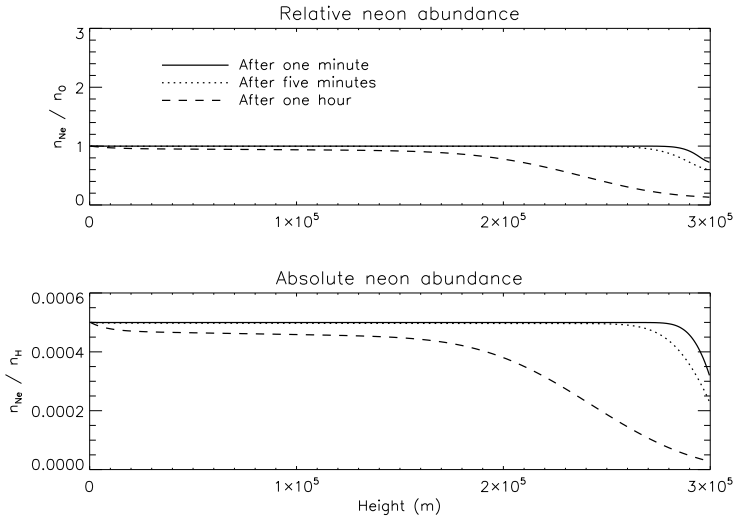

Figure 5.3: The absolute and relative neon abundances with enhanced neon ionisation rate in model C.

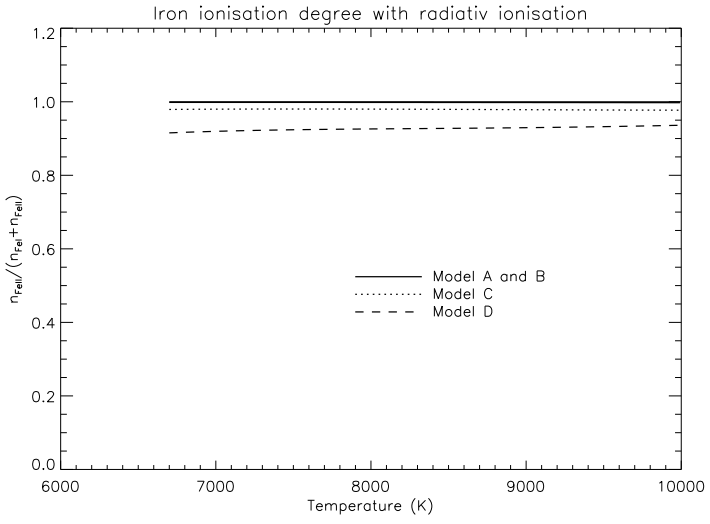

Figure 5.4: The iron ionisation degree in model A, B, C and D with the radiative ionisation rate of von Steiger and Geiss (1989) in addition to the collisional ionisation rate. The ionisation degrees of models A and B overlap.

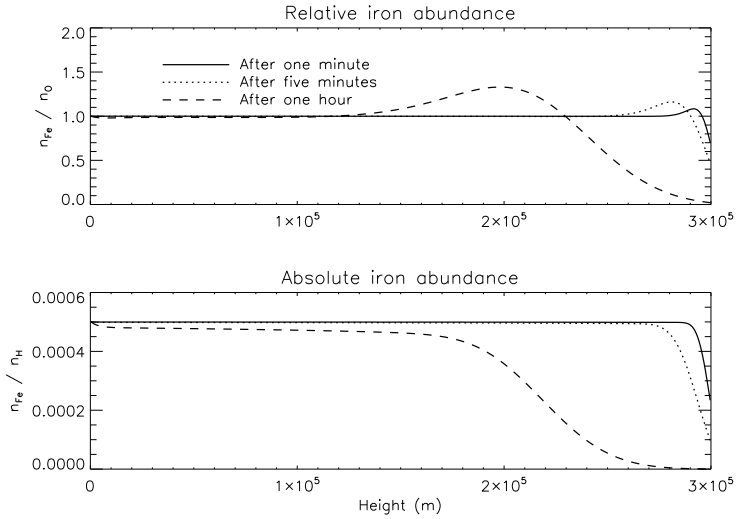

Figure 5.5: The absolute and relative iron abundances with enhanced iron ionisation rate in model A.

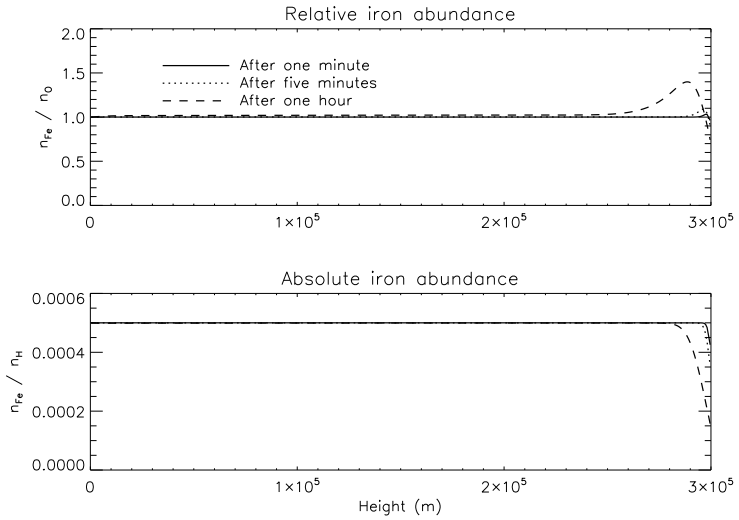

Figure 5.6: The absolute and relative iron abundances with enhanced iron ionisation rate in model C.

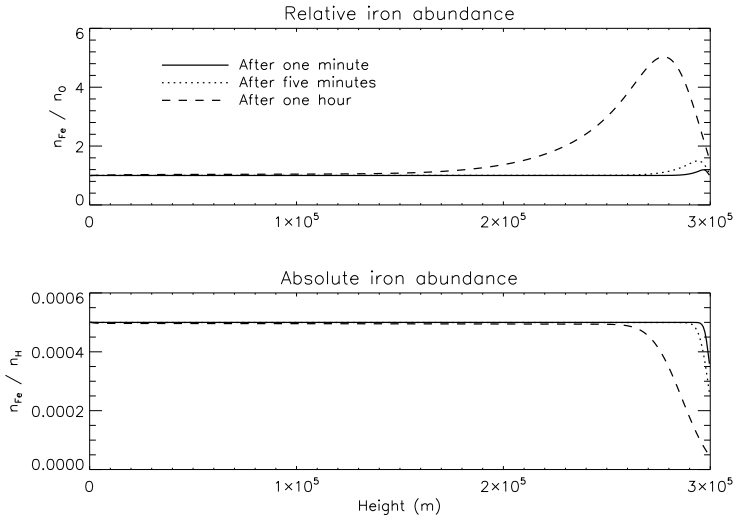

Figure 5.7: The absolute and relative iron abundances with enhanced iron ionisation rate in model B.

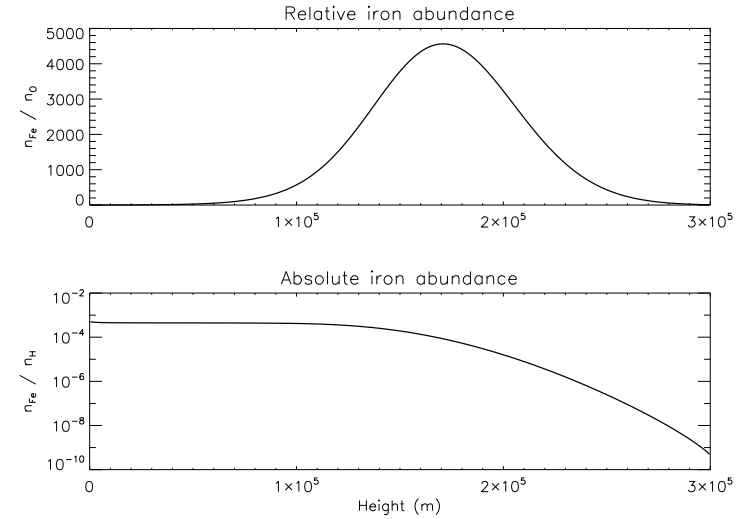

Figure 5.8: Maximum relative iron abundance with enhanced iron ionisation rate in model B, reached at 5×10^4s. The correspondent absolute abundance is shown in the lower panel.

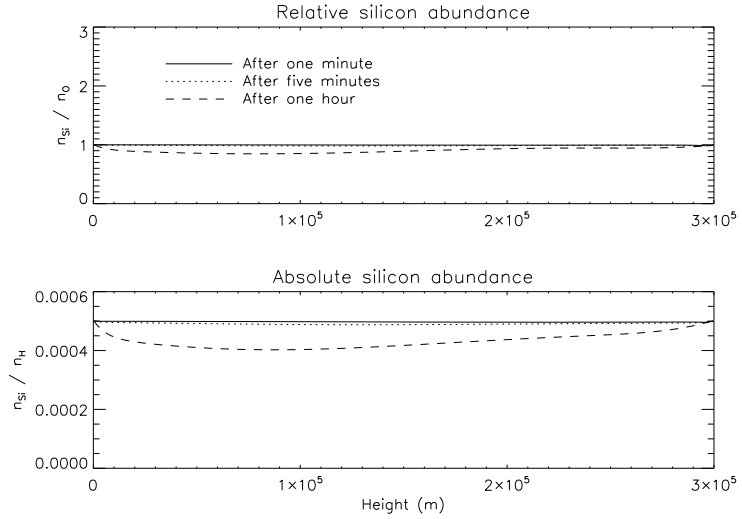

Figure 5.9: The absolute and relative silicon abundances obtained when gas with photospheric silicon (and oxygen) abundance is flowing into the grid from the overlying layer. Background model B is used.

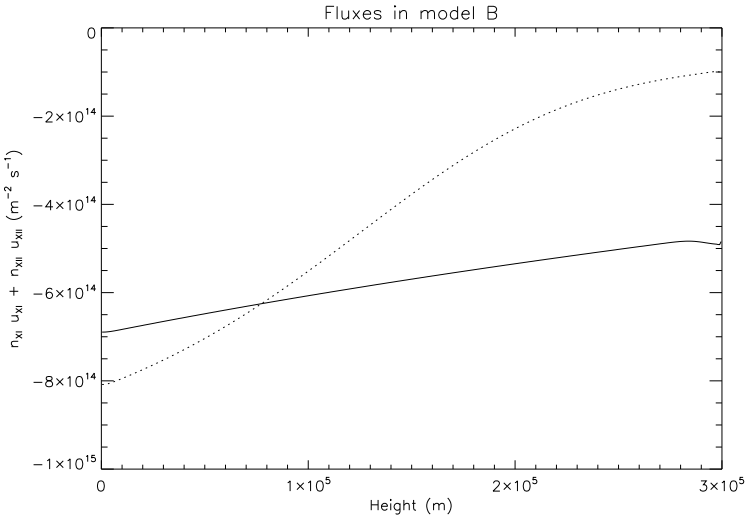

Figure 5.10: The oxygen (solid curve) and silicon (dotted curve) fluxes after one minute for the solution shown in figure 5.9.

general (absolute abundance enhancement of iron), the present work cannot be the correct explanation for the observed FIP fractionation. However, observations of coronal streamers by Raymond et al. (1997a) show no evidence for absolute abundance enhancement of low FIP elements. We therefore conclude that we cannot know if the low FIP elements really are enriched in the corona compared to the photosphere.

One of the main results of this study is that the abundance enhancement of the low FIP elements (e.g. silicon) compared to oxygen is highly dependent on the ionisation degree of the background. We have seen that the background ionisation degree cannot be too low, nor too high, in order to obtain FIP fractionation. The maximum enhancement is obtained in model B, i.e. in a layer where the background is approximately 5% - 10% ionised.

In order to understand why this is so, one has to keep in mind the strong relation between the ionisation degrees of oxygen and hydrogen (see equation 4.8) due to the charge exchange interaction between these two elements. Consequently, the more ionised hydrogen we have, the more ionised oxygen we have, and the slower the gravitational settling of oxygen is. When oxygen flows slower than the low FIP element, no enhancement of the latter compared to oxygen is produced. On the other hand, the flow of the low FIP element is also delayed by collisions with protons, and the more protons we have, the slower the gravitational settling of the low FIP element is. If there are too few protons for the low FIP element to collide with, Coulomb collisions will no longer dominate the force balance and since the neutral-neutral collision frequency is of the same magnitude as the neutral-ion collision frequency[1], heavier elements will simply fall faster than lighter ones, independently on their ionisation degrees. If our collision frequencies are wrong, and the ion-neutral collisions should be more frequent than the neutral-neutral collisions, we could imagine a FIP fractionation that takes place even in a completely neutral background (such as model E defined below), because the low FIP elements are ionised but oxygen is not.

In order to illustrate the importance of the background ionisation degree, we have used background models with ionisation degrees up to 84%. At the same time we claim to model the chromosphere. In reality this is a

[1]The neutral-neutral collision frequency between oxygen and hydrogen is larger than the collision frequencies of both types of neutral-ion collisions between these two elements, $\nu_{\mathrm{OII-H}} < \nu_{\mathrm{OI-p}} < \nu_{\mathrm{OI-H}}$. For the low FIP elements (Mg, Si and Fe), the collisions between neutral Si (Mg, Fe) and protons are more frequent than the neutral-neutral collisions between Si (Mg, Fe) and hydrogen, while the collisions between neutral hydrogen and ionised Si (Mg, Fe) are less frequent, i.e. $\nu_{\mathrm{SiII-H}} < \nu_{\mathrm{SiI-H}} < \nu_{\mathrm{SiI-p}}$. Since we now refer to a background without protons, neutral-neutral collisions dominate over the neutral-ion collision also for the low FIP elements.

contradiction, because when the hydrogen gas is almost fully ionised it is not able to lose energy through radiation (too few bounded electrons). The gas consequently heats rapidly and becomes transition region- or coronal gas. The hydrogen gas in model C and D is not really chromospheric and these two models do therefore not constitute realistic simulations of the situation we want to study in this work. The only reason why we are able to implement high ionisation degrees and low temperatures simultaneously in this study, is because we do not solve the energy equation.

For iron an abundance enhancement is only achieved in model B, while for silicon and magnesium an enhancement is obtained in model A and C as well. Since no elements are enriched in model D, we already have an upper limit for the background ionisation degree, but we need to check that there also exists a lower limit and that the FIP fractionation disappears when there are no protons in the background.

Let us therefore add a fifth background model, labelled E, to our set of models (A, B, C and D), where the hydrogen ionisation degree is zero. We obtain an ionisation degree $\frac{n_p}{n_H+n_p} < 0.01\%$ by letting the proton density be 10^{-4} of the neutral hydrogen density at the lower boundary at $t = 0$, and letting the initial neutral and ionised hydrogen densities be given by their respective hydrostatic equilibrium densities. The ionisation rate is set to $10^{-10}\mathrm{s}^{-1}$ while the recombination rate is given by the same equation as for the other models. As shown in figure 5.1, we do not get any relative abundance enhancement of silicon compared to oxygen in this new model. In fact, the ionised silicon velocity is a factor of $4 \sim 5$ higher (in absolute value) than in model A, and both neutral and ionised silicon fall faster than neutral oxygen in this model. The ionised oxygen velocity is insignificant because the oxygen ionisation degree is close to zero (less than 0.01%).

We have already mentioned that, in order to produce relative abundance enhancement with gravitational settling as in this study, the chromospheric gas has to be mixed regularly. In fact, the obtained FIP fractionation depends on how often such mixing process occurs. The time interval between two successive mixing processes cannot be too short, nor too long. With the strong abundance enhancement of silicon and magnesium obtained in model B, we can theoretically produce any FIP fractionation we want by choosing the right time interval for the mixing process. The problem is that if we choose very long time intervals, both the low FIP element and oxygen are highly depleted relative to hydrogen. The composition we obtain could therefore be rather unrealistic even if the FIP fractionation would fit with the observed relative abundances.

If we go back to the silicon results in section 4.2.2, we see that the maxi-

mum abundance enhancement after five minutes is ~ 1.1 in model A, ~ 1.5 in model B and ~ 1.05 in model C. This means that if the time scale for the mixing process is approximately five minutes, the FIP fractionation is basically absent, taking into account that one has to make an average in time and space of the obtained abundance enhancements. Even the maximum values are small compared to the observed FIP fractionation presented in chapter 1. We therefore have to assume longer time intervals for the mixing process. In model C, we do not achieve any significant FIP fractionation for silicon even if we choose one hour long time intervals between the mixing processes, but in model A and B such time intervals yield a silicon FIP fractionation of roughly $\mathcal{F} \sim 2$ and $\mathcal{F} \sim 3$ respectively, if we do a rough average over a height interval, labelled ℓ, corresponding to the upper third of our grid. After one hour of gravitational settling in model A, the absolute abundances of silicon and magnesium in the height interval ℓ are depleted by approximately a factor of three, i.e. $\mathcal{A}(X)^{upper\ atmosphere} \sim 2 \times 10^{-4}$ compared to the photospheric abundance $\mathcal{A}(X)^{photosphere} = 5 \times 10^{-4}$ (where X = Si, Mg). At the same heights and after the same time interval, in model B these elements are depleted by approximately a factor of two, $\mathcal{A}(X)^{upper\ atmosphere} \sim 3 \times 10^{-4}$, while oxygen is depleted by roughly a factor of five in both model A and B, $\mathcal{A}(O)^{upper\ atmosphere} \sim 10^{-4}$. This result is not too far from what Raymond et al. (1997a) found when studying elemental abundances in coronal streamers (at a height $0.5R_\odot$ above the solar limb), and it could imply that the depletion they found is not due to gravitational settling within the streamer, but rather in the chromospheric layer below.

With a time scale of one hour as discussed above, or even time scales of half an hour, the very short settling time for neon leads to an enhancement of the relative abundance ratio $\mathcal{R}(\frac{\mathrm{Mg}}{\mathrm{Ne}}) > 20$ between magnesium and neon, while a mixing process each 20 minutes yields an enhancement factor of < 10 for the same abundance ratio. The latter could fit with the abundances derived from observations of a polar plume by Widing and Feldman (1992) (see chapter 1), but observation of the corona above quiet sun regions by Young (2005) yielded an enhancement of < 2 for the same ratio, which in our case is reproduced only with very small time intervals (less than five minutes) for the mixing process.

The obtained FIP fractionation does not only depend on the ionisation degree of the background (and hence on the ionisation degree of oxygen) and the rate of occurrence for the mixing process. The FIP fractionation also depends on the ionisation degree of the minor constituent itself. The only high FIP element we study in this work, except oxygen, is neon (FIP = 21.6 eV) and has approximately zero ionisation degree in all four background models (see figure 4.38). In model B, the relative neon abundance $\mathcal{R}(\frac{\mathrm{Ne}}{\mathrm{O}})$ is depleted

by a factor of ~ 40 at the upper boundary after one hour, and the absolute neon abundance $\mathcal{A}(\mathrm{Ne})$ is depleted by a factor of ~ 600 (see figure 4.39). These are much lower densities than what the measurements of the relative abundance ratio $\mathcal{R}(\frac{\mathrm{Mg}}{\mathrm{Ne}})$, presented in chapter 1, indicate. We therefore want to see what happens with the abundances of the high FIP element neon if we add radiative ionisation to its ionisation rate. To do this, we use the radiative ionisation rate of von Steiger and Geiss (1989). This rate is constant, $R_{12} = 1.24 \times 10^{-2}$ s^{-1} for neon, while the recombination rate depends on the electron (proton) density. Hence, since the background ionisation degree increases significantly from model A to D, the recombination rate for neon also increases and the neon ionisation degree decreases. Since there is no reason why the radiative ionisation rate for neon, should be larger than the one for hydrogen, we need to check the radiative ionisation rates for hydrogen in the four models. The latter are given in table 4.1, and with the ionisation rate for neon given above, it only makes sense to use background model C or D. The ionisation degree of neon in model C, with both radiative and collisional ionisation, is shown in figure 5.2. The absolute and relative neon abundances in figure 5.3 show that we do not get any enrichment of neon compared to oxygen even when their ionisation degrees are similar, but the relative and absolute neon abundances are now only depleted by a factor of ~ 8 and ~ 20, respectively. Since the absolute magnesium abundance is depleted by a factor of ~ 2 in the upper part of the grid, as shown in table 4.4 (and by a factor of ~ 5 at the upper boundary), this neon abundance actually fits quite well with the relative Mg/Ne abundance ratios determined by Widing and Feldman (1992) and Young (2005).

Regarding iron, the results in section 4.2.4 show that we only obtain an enhancement of the abundance ratio Fe/O in model B (see figure 4.34). We therefore increase the ionisation degree of iron, by adding radiative ionisation, and study what effect this has on the abundances. If we, as for neon, use the radiative ionisation rate of von Steiger and Geiss (1989) (which for iron is $R_{12} = 1.1$ s^{-1}) in addition to the old ionisation/recombination rates, the extremely high ionisation degrees shown in figure 5.4 are produced. Due to the very low proton (electron) density in model A and B, the ratio $P_{21}/P_{12} = n_1/n_2$ is approximately 10^{-4} and 10^{-3}, respectively, and hence, the ionisation degree $\frac{n_2}{n_1+n_2} \sim \frac{n_2}{n_2} = 100\%$ in both these two models. The abundances in figure 5.5 and 5.6 show that we achieve a small enhancement of iron compared to oxygen also in model A and C, respectively, when the ionisation degrees are as shown in figure 5.4. Figure 5.7 shows that the iron abundance enhancement in model B, with an iron ionisation degree of $\sim 100\%$, is increased by approximately a factor of ~ 3 ($\mathcal{F} \sim 5$ compared to $\mathcal{F} < 1.5$) after one hour. The maximum value of the relative abundance $\mathcal{R}(\frac{\mathrm{Fe}}{\mathrm{O}})$ in model

B is also much higher than (approximately 3000 times) the case with only collisional ionisation, as shown by figure 5.8. The question remains why we should include radiative ionisation for some elements (Fe and Ne) and not for others (Mg, Si and O). However, if we add radiative ionisation to the ionisation rates of all the elements, the results we obtain are not too different from the ones presented in chapter 4. In fact, the ionisation process of oxygen is still dominated by the charge exchange with hydrogen, and no new results are obtained. If we add the radiative ionisation rate of von Steiger and Geiss (1989) (which for silicon is $R_{12} = 0.92$ s^{-1}) to the silicon ionisation rate, we obtain an ionisation degree of silicon that is approximately 100% through the whole grid. However, the maximum value of the relative silicon abundance enhancement after one hour is only $\mathcal{F} \sim 6.5$, compared to the old value $\mathcal{F} \sim 4.3$, and hence it can still be compared with the observed results. The same is valid for magnesium. The conclusion is that radiative ionisation has to be taken into account for all the minor constituents.

Finally we want to check the importance of the upper boundary condition. We have set the minor constituent velocities to zero at the upper boundary, and we thereby do not let particles enter the slab from above. Now we change the upper boundary condition for the minor constituents in the background model B. We let material of photospheric composition continuously flow into the slab from the overlying layer. This is obtained by using a constant density $\mathcal{A} = 5 \times 10^{-4}$ for all minor constituents (and hence a constant pressure) as the upper boundary condition for the momentum equation. When the gas starts to settle in the gravitational field, this constant pressure leads to an increasing pressure gradient that allows the gas to flow into the grid. Figure 5.9 shows that we do not obtain any enrichment of silicon compared to oxygen with this boundary condition, but we neither achieve any significant depletion of the relative or absolute silicon abundances. The absolute abundance is at most depleted by a factor of 1.3 during the first hour of gravitational settling, and no depletion takes place at the boundaries. Figure 5.10 shows that the oxygen flux is larger, in magnitude, than the silicon flux in the upper part of the grid (as was the case also with the old boundary conditions, cf. figure 4.18), but since both silicon and oxygen are supplied with silicon- and oxygen rich material, respectively, their absolute abundances remain constant in time at the upper boundary. Hence, the oxygen velocity is larger, in absolute value, than the silicon velocity. The absolute abundances at the lower boundary are fixed.

This tells us that, in order to achieve an enrichment of low FIP elements compared to high FIP elements as seen in section 4.2, the gravitational settling has to take place in the upper chromosphere, just below the transition region. In fact, as long as we have constant thermal conduction from the

corona to the transition region, the flow of the minor constituents from the lower transition region down to the chromosphere is prevented by the thermal forces in the transition region (Killie and Lie-Svendsen, 2007). Setting the minor constituent velocities to zero at the upper boundary therefore makes sense only if we study gravitational settling in a well mixed chromosphere layer just below the transition region, and not in lower layers of the chromosphere where the minor constituents can enter the slab from above.

Chapter 6

Summary

We have studied gravitational settling of minor, heavy, constituents in a well mixed chromosphere. In such a chromosphere, the minor constituent abundances deviate strongly form their hydrostatic equilibrium abundances. They therefore, due to gravity, fall towards the sun, ending up with abundances (constant in time) that are close to their hydrostatic equilibrium abundances. These abundances, due to the small scale heights of the minor constituents, are all highly depleted compared to the observed abundances, and heavier elements have abundances that are many orders of magnitude smaller than lighter ones, in the upper part of the grid, independently on the FIP. We have therefore focused on the first hour of the gravitational settling, assuming that some mixing process regularly takes place in order to continuously repeat the settling process. We also assume that the gas in the upper chromosphere is repeatedly transported up to the corona, where the abundances we compare with are measured.

We found that whether or not low FIP elements are enriched compared to the high FIP element oxygen, and by how much they eventually are enriched, depend on the ionisation degree of oxygen, that again is determined by the ionisation degree of the background. When the ionisation degree of the background (and oxygen) is low ($\sim 5\%$), the friction between oxygen and the background is small. Oxygen therefore settles faster than the highly ionised low FIP elements, who feel a stronger frictional force from the background (Coulomb collisions). An enhancement (with respect to the photosphere) of the relative abundances $\mathcal{R}(\frac{\mathrm{Mg}}{\mathrm{O}})$ and $\mathcal{R}(\frac{\mathrm{Si}}{\mathrm{O}})$, comparable with the observed abundances, is achieved if we assume that a mixing process occurs approximately once an hour.

The low FIP element iron is twice as heavy as the other two, and the friction between the iron gas and the background requires more ionised iron (higher iron ionisation degree) in order to obtain an iron velocity significantly

smaller (in absolute value) than the oxygen velocity. In fact, with only collisional (direct) iron ionisation, the enhancement of the abundance ratio Fe/O is almost negligible, even in a $\sim 5\%$ ionised background. However, with a radiative ionisation rate that yields an iron ionisation degree of 100% in a $\sim 5\%$ ionised background, we achieve an enhancement of the relative abundance $\mathcal{R}(\frac{\mathrm{Fe}}{\mathrm{O}})$ that can be compared with the observed abundances. The ionisation rate of the high FIP element neon also needs to be strongly enhanced (by adding radiative ionisation) in order to produce neon abundances that are not too low compared to the observed ones. In order to be consistent, we therefore also include radiative ionisation for silicon and magnesium, and the abundance enhancements obtained can still be compared with the observed ones.

We conclude that the mechanism studied in this thesis does work quite well if the ionisation degree is *high* ($\sim 100\%$) for the low FIP elements and *low* ($< 10\%$) for the hydrogen background and the high FIP element oxygen. Furthermore, the ionisation degree of the high FIP element neon cannot be too low ($> 20\%$).

Bibliography

Abramowitz, M. and Stegun, I. A. (1964). *Handbook of mathematical functions*. U.S. Department of Commerce, third edition.

Anders, E. and Grevesse, N. (1989). Abundances of the elements - Meteoritic and solar. volume 53, pages 197–214.

Arnaud, M. and Raymond, J. (1992). Iron ionization and recombination rates and ionization equilibrium. *ApJ*, 398:394–406.

Arnaud, M. and Rothenflug, R. (1985). An updated evaluation of recombination and ionization rates. *A&AS*, 60:425–457.

Asplund, M., Grevesse, N., Sauval, A. J., Allende Prieto, C., and Kiselman, D. (2004). Line formation in solar granulation. IV. [O I], O I and OH lines and the photospheric O abundance. *A&A*, 417:751–768.

Banks, P. M. and Kockarts, G. (1973). *Aeronomy*. Academic Press, Inc. New York.

Biemont, E. and Grevesse, N. (1977). F-values and abundances of the elements in the sun and stars. *Physica Scripta*, 16:39–47.

Gray, D. F. (2005). *The observation and analysis of the stellar atmospheres*. Cambridge University Press, New York.

Grevesse, N. and Sauval, A. J. (1998). Standard Solar Composition. *Space Science Reviews*, 85:161–174.

Hansteen, V. H., Leer, E., and Holzer, T. E. (1997). The Role of Helium in the Outer Solar Atmosphere. *ApJ*, 482:498–+.

Hénoux, J.-C. (1998). FIP Fractionation: Theory. *Space Science Reviews*, 85:215–226.

Henoux, J. C. and Somov, B. V. (1997). The photospheric dynamo. I. Physics of thin magnetic flux tubes. *A&A*, 318:947–956.

Hummer, D. G. (1983). The generalized exponential-integral. *Journal of Quantitative Spectroscopy and Radiative Transfer*, 30:281–287.

Killie, M. A. and Lie-Svendsen, Ø. (2007). Modeling Minor Ion Abundances in Quiescent Coronal Loops. *ApJ*, 666:501–515.

Korevaar, P. and van Leer, B. (1988). Time-dependent corona models - A numerical method. *A&A*, 200:153–167.

Lie-Svendsen, Ø. and Esser, R. (2005). Modeling the Energy Budget of Solar Wind Minor Ions: Implications for Temperatures and Abundances. *ApJ*, 618:1057–1073.

Marsch, E., von Steiger, R., and Bochsler, P. (1995). Element fractionation by diffusion in the solar chromosphere. *A&A*, 301:261–+.

Meyer, J.-P. (1985). Solar-stellar outer atmospheres and energetic particles, and galactic cosmic rays. *ApJS*, 57:173–204.

Mogro-Campero, A. and Simpson, J. A. (1972). Enrichment of Very Heavy Nuclei in the Composition of Solar Accelerated Particles. *ApJL*, 171:L5+.

Peter, H. (1998). Element fractionation in the solar chromosphere driven by ionization-diffusion processes. *A&A*, 335:691–702.

Press, W., S.A.Teukolsky, Vetterling, W., and Flannery, B. (1992). *Numerical Recipes in Fortran 77*. Cambridge University Press.

Raymond, J. C., Kohl, J. L., Noci, G., Antonucci, E., Tondello, G., Huber, M. C. E., Gardner, L. D., Nicolosi, P., Fineschi, S., Romoli, M., Spadaro, D., Siegmund, O. H. W., Benna, C., Ciaravella, A., Cranmer, S., Giordano, S., Karovska, M., Martin, R., Michels, J., Modigliani, A., Naletto, G., Panasyuk, A., Pernechele, C., Poletto, G., Smith, P. L., Suleiman, R. M., and Strachan, L. (1997a). Composition of Coronal Streamers from the SOHO Ultraviolet Coronagraph Spectrometer. *Solar Physics*, 175:645–665.

Raymond, J. C., Suleiman, R. M., van Ballegooijen, A. A., and Kohl, J. L. (1997b). Absolute Abundances in Streamers from UVCS. In Wilson, A., editor, *Correlated Phenomena at the Sun, in the Heliosphere and in Geospace*, volume 415 of *ESA Special Publication*, pages 383–+.

Russell, H. N. (1929). On the Composition of the Sun's Atmosphere. *ApJ*, 70:11–+.

Rutten, R. J. (1999). *Radiative Transfer in Stellar Atmospheres*. lecture notes, Utrecht University, first esmn edition.

Schultz, D. R., Krstic, P. S., Lee, T. G., and Raymond, J. C. (2008). Momentum Transfer and Viscosity from Proton-Hydrogen Collisions Relevant to Shocks and Other Astrophysical Environments. *ApJ*, 678:950–960.

Schunk, R. W. (1977). Mathematical structure of transport equations for multispecies flows. *Reviews of Geophysics and Space Physics*, 15:429–445.

Shull, J. M. and van Steenberg, M. (1982). The ionization equilibrium of astrophysically abundant elements. *ApJS*, 48:95–107.

Vauclair, S. (1996). Element segregation in the solar chromosphere and the FIP bias: the "Skimmer" model. *A&A*, 308:228–232.

Vernazza, J. E., Avrett, E. H., and Loeser, R. (1981). Structure of the solar chromosphere. III - Models of the EUV brightness components of the quiet-sun. *ApJS*, 45:635–725.

von Steiger, R. and Geiss, J. (1989). Supply of fractionated gases to the corona. *A&A*, 225:222–238.

von Steiger, R., Schweingruber, R. F. W., Geiss, J., and Gloeckler, G. (1995). Abundance variations in the solar wind. *Advances in Space Research*, 15:3–.

Wang, Y.-M. (1996). Element Separation by Upward Proton Drag in the Chromosphere. *ApJL*, 464:L91+.

White, S. M., Thomas, R. J., Brosius, J. W., and Kundu, M. R. (2000). The Absolute Abundance of Iron in the Solar Corona. *ApJL*, 534:L203–L206.

Widing, K. G. (1997). Emerging Active Regions on the Sun and the Photospheric Abundance of Neon. *ApJ*, 480:400–+.

Widing, K. G. and Feldman, U. (1989). Abundance variations in the outer solar atmosphere observed in SKYLAB spectroheliograms. *ApJ*, 344:1046–1050.

Widing, K. G. and Feldman, U. (1992). Element abundances and plasma properties in a coronal polar plume. *ApJ*, 392:715–721.

Young, P. R. (2005). The element abundance FIP effect in the quiet Sun. *A&A*, 439:361–366.